submitted to *Geophys. J. Int.*

Navigating the space of seismic anisotropy for crystal and whole-Earth scales

Aakash Gupta[1], Carl Tape[1], J. Michael Brown[2] and Thorsten W. Becker[3,4,5]

[1] *Geophysical Institute and Department of Geosciences, University of Alaska Fairbanks, 2156 Koyukuk Drive, Fairbanks, Alaska, 99775, U.S.A.*

[2] *Department of Earth and Space Sciences, University of Washington, Seattle, Washington, 98195, U.S.A.*

[3] *Institute for Geophysics, Jackson School of Geosciences, The University of Texas at Austin, 10100 Burnet Road, Austin, Texas, 78758, U.S.A.*

[4] *Department of Earth and Planetary Sciences, Jackson School of Geosciences, The University of Texas at Austin, 10100 Burnet Road, Austin, Texas, 78758, U.S.A.*

[5] *Oden Institute for Computational Engineering and Sciences, The University of Texas at Austin, 201 E 24th St., Austin, Texas, 78712, U.S.A.*

27 January 2025

SUMMARY

Evidence of seismic anisotropy is widespread within the Earth, including from individual crystals, rocks, borehole measurements, active-source seismic data, and global seismic data. The seismic anisotropy of a material determines how wave speeds vary as a function of propagation direction and polarization, and it is characterized by density and the elastic map, which relates strain and stress in the material. Associated with the elastic map is a symmetric 6×6 matrix, which therefore has 21 parameters. The 21-dimensional space of elastic maps is vast and poses challenges for both theoretical analysis and typical inverse problems. Most estimation approaches using a given set of directional wavespeed measurements assume a high-symmetry approximation, typically either in the form of isotropy (2 parameters), vertical transverse isotropy (radial anisotropy: 5 parameters), or horizontal transverse isotropy (azimuthal anisotropy: 6 parameters). We offer a general approach to explore the space of elastic maps by starting with a given elastic map $\mathbf{T}$. Using a combined minimization and projection procedure, we calculate the closest Σ-maps to $\mathbf{T}$, where Σ is one of the eight elastic symmetry classes: isotropic, cubic, transverse isotropic, trigonal, tetragonal, orthorhombic, monoclinic, and trivial. We apply this approach to 21-parameter elastic maps derived from laboratory measurements of minerals; the measurements include dependencies on pressure, temperature, and composition. We also examine global elasticity models derived from subduction flow modeling. Our approach offers a different perspective on seismic anisotropy and motivates new interpretations, such as for why elasticity varies as a function of pressure, temperature, and composition. The two primary advances of this study are 1) to provide visualization of elastic maps, including along specific pathways through the space of model parameters, and 2) to offer distinct options for reducing the complexity of a given elastic map by providing a higher-symmetry approximation or a lower-anisotropic version. This could contribute to improved imaging and interpretation of Earth structure and dynamics from seismic anisotropy.

Key words: seismic anisotropy, elasticity, computational seismology

1 INTRODUCTION

Composition and elasticity are two fundamental properties of solid materials. These may be natural materials—as in a mineral, rock, or continental-scale portion of the Earth—or they may be manmade, as in the case of concrete aggregates, alloys, or chemical structures generated in a laboratory. Generally speaking, elasticity characterizes how a solid material deforms under stresses. One type of applied stress is an elastic wave, which propagates as a compressional wave or a shear wave. The directional dependence of wave speeds is known as seismic anisotropy.

The elasticity of a material is expressed by its elastic map—a function that relates stress to strain (Eq. 1). Associated with the elastic map is its 6×6 matrix representation. The matrix is symmetric and hence is determined by 21 parameters. A fundamental pursuit is to characterize the elastic symmetry of a material, so as, for example, to understand direction-dependent wave speed variations or infer past deformation conditions from crystallographic preferred orientation (CPO) anisotropy. The notion of elastic symmetry will play an important role. There are eight possible elastic symmetry classes (Forte & Vianello 1996): isotropic (ISO), cubic (CUBE), transverse isotropic (XISO), trigonal (TRIG), tetragonal (TET), orthorhombic (ORTH), monoclinic (MONO), and trivial (TRIV). For an isotropic material, any rotation of the material leaves the elastic map unchanged. For a trivial material, no rotation—other than of course the identity—leaves the elastic map unchanged.

Our motivation is to better understand the elasticity of natural materials, from a mm-scale mineral (or crystal) measured in a lab to the entire Earth. Evidence of seismic anisotropy is widespread in Earth (e.g. Maupin & Park 2007; Mainprice 2007; Montagner 2007; Long & Becker 2010), including individual crystals (Angel et al. 2009; Almqvist & Mainprice 2017), rock samples (Johnston & Christensen 1995; Brownlee et al. 2017), borehole data (Okaya et al. 2004; Kästner et al. 2020), active-source seismic data (Hess 1964; Helbig 1994), and global seismic data (Nataf et al. 1984; Montagner & Tanimoto 1991). Even PREM, a 1D description of Earth, has radial anisotropy in the uppermost mantle to account for Rayleigh-Love wave speed discrepancies (Dziewonski & Anderson 1981). Anisotropy can arise from shape preferred orientation including the average effect of layered, different speed isotropic materials (Backus 1962), crystallographic preferred orientation of instrinsically anisotropic crystals such as olivine under deformation (Karato et al. 2008), and dilational cracks in the crust (Crampin 1987).

In a laboratory setting, one may have the benefit of excellent coverage of measurement directions for a homogeneous material such as a mineral with known chemistry. Or instead of a mineral, the material may be a rock sample having multiple minerals that may or may not be aligned and may or may not have microcracks.

The step in scale from a laboratory experiment to an active-source field experiment, such as for oil and gas exploration, involves an increase in heterogeneity, a reduction in the quality of measurement coverage of the target domain, and a diminished knowledge of the composition of the subsurface units. (A limited number of wells may provide rock samples for a small part of the target domain.)

The step in scale from an active-source field experiment to a typical passive seismic imaging experiment using ambient noise and earthquakes involves further reduction of available information, resulting in greater challenges. For example, the distribution of global seismometers at the surface is irregular and sparse, the subsurface heterogeneity is extreme in places (e.g., the corner flow above a subducting slab), and there is no direct access to materials at depths of tens to thousands of km (though surface rocks originating from these depths provide insights).

The different settings for laboratory, active-source, and global experiments lead to different capabilities for estimating the elastic properties of homogeneous or heterogeneous media. At global and continental scales, studies and applications have considered parameterizations for complex anisotropy (Montagner & Nataf 1986; Montagner & Tanimoto 1991; Becker et al. 2006; Panning & Nolet 2008; Chen et al. 2007; Russell et al. 2022; Eddy et al. 2022), but sparse data coverage has limited most studies to assume isotropic or transverse isotropic properties. The most common assumption is that the axis of symmetry for the transversely isotropic (XISO) material is either vertical (VTI; radial anisotropy) or horizontal (HTI; azimuthal anisotropy), rather than the case of tilted transverse isotropy (TTI), which has been applied at regional scales (Abt et al. 2009; Monteiller & Chevrot 2011; Liu & Ritzwoller 2024).

Active-source field experiments, targeting sedimentary units such as shale with dense surface coverage of sensors, have enabled the estimation of transversely isotropic and orthorhombic properties (Operto et al. 2009; Fletcher et al. 2009; Bakulin et al. 2010; Alkhalifah & Plessix 2014; Hadden & Pratt 2017; Oh et al. 2020; Ye et al. 2023). These seismic imaging experiments benefit from direct measurements of wave speeds from rock samples collected at the surface or from well logs. At the laboratory scale, ultrasonic measurements have been used for decades to characterize elastic properties (Verma 1960; Birch 1961; Christensen 1966). One approach involves preparing spherical samples and measuring travel times for dozens of different paths through the material (Pros & Babuška 1968; Vestrum et al. 1996; Lokajíček & Svitek 2015; Lokajíček et al. 2021). This enables all 21 elastic parameters to be estimated, and, depending on the uncertainties, the material may or may not exhibit 21-parameter (TRIV) anisotropy.

The geophysical estimation (or inverse) problem depends on the target material, the measurements, and the chosen parameterization of the material, both for the type of material (its elastic symmetry) and for how the material varies in the volume (e.g., a volumetric grid of cells or spherical harmonic functions). These factors are interrelated. For example, at a laboratory scale, one might perform a limited number of ultrasonic measurements of a crystal. The choice of elastic parameters to estimate could be isotropic (two parameters), in which case the estimation problem may be stable, or it could be 21 parameters, in which case the estimation problem is highly underdetermined and the solution is characterized by a large range of solutions. The choice of measurements and parameterization would likely be informed by the material, with more measurements and more parameters needed for feldspar crystals, which have low elastic symmetry (Brown et al. 2016), and fewer measurements for garnets, which have high-elastic symmetry (Jiang et al. 2004). Or one might choose to make more measurements and consider a full parameterization, even if the sample is assumed to have higher symmetry, such as granite (Lokajíček et al. 2021); this results in a less-biased determination of elastic symmetry.

For active-source or global settings, the inverse problem is far more extreme than the case of the laboratory setting, on account of heterogeneity, sparse data coverage, and unknown source parameters. One example of the complexities of global imaging is the trade off between estimating isotropic and anisotropic structures. This can be challenging even for radial anisotropy (VTI) for surface wave imaging (Laske & Masters 1998; Ekström 2011), and it is compounded by source parameter uncertainty (Ma & Masters 2015).

Our study provides a framework for studying elastic materials (Section 4), with different objectives for laboratory experimentalists and seismologists. The applications in Section 3 show how distances to symmetry classes provide a tool to guide fundamental interpretations, such as the assessment of elastic symmetry for a measured rock sample. In some cases, the framework will offer a simpler and more accurate interpretation. For seismologists, who face sparser data coverage and stronger heterogeneity compared with laboratory settings, the current choices of regularization to stabilize the seismic imaging inverse problem could be formalized to account for the choice of elastic symmetry parameterization, as we suggest in Section 5. Regularization may involve biasing models from the most complex (21 parameters) to the simplest (2 parameters), and these decisions require an understanding of the available pathways in between these endmembers in the space of model parameters. Hence our focus is on the exploration of the 21-parameter space of elasticity, as well as the potential benefits to laboratory, field, and global settings.

2 VISUALIZING ELASTIC MAPS AND THE DISTANCES AMONG THEM

Linear elasticity is mathematically represented as an elastic map, that is, a self-adjoint linear map

$$\mathbf{T}(\boldsymbol{\varepsilon}) = \boldsymbol{\sigma} \tag{1}$$

that transforms a 3×3 strain matrix $\boldsymbol{\varepsilon}$ to a 3×3 stress matrix $\boldsymbol{\sigma}$. One can choose an orthonormal set of six 3×3 symmetric matrices as a basis $\mathbb{B}$ for the space of all 3×3 symmetric matrices (i.e., strains or stresses). Then from Equation (1),

$$[\mathbf{T}]_{\mathbb{BB}}[\boldsymbol{\varepsilon}]_{\mathbb{B}} = [\boldsymbol{\sigma}]_{\mathbb{B}}, \tag{2}$$

where $[\mathbf{T}]_{\mathbb{BB}}$ is the (6×6) matrix of $\mathbf{T}$ with respect to $\mathbb{B}$, and where $[\boldsymbol{\varepsilon}]_{\mathbb{B}}$ and $[\boldsymbol{\sigma}]_{\mathbb{B}}$ are the (6×1) coordinate vectors of ϵ and σ with respect to $\mathbb{B}$. The matrix $[\mathbf{T}]_{\mathbb{BB}}$ is symmetric since $\mathbf{T}$ is self-adjoint and since $\mathbb{B}$ is orthonormal. In this paper we use the basis $\mathbb{B}$ of Tape & Tape (2021, eq. 3). Appendix A explains why the resulting matrix $[\mathbf{T}]_{\mathbb{BB}}$ is preferable to the traditional Voigt matrix of $\mathbf{T}$.

For each elastic map $\mathbf{T}$, we calculate its *monoclinic angle function* as (Tape & Tape 2024, eq. 22)

$$\alpha_{\text{MONO}}(\mathbf{v}) = \alpha^{\mathbf{T}}_{\text{MONO}}(\mathbf{v}) = \angle\left(\mathbf{T}, \mathbf{P}\left(\mathbf{T},\ \boldsymbol{\mathcal{V}}_{\text{MONO}}(\mathbf{v})\right)\right), \tag{3}$$

where $\mathbf{P}(\mathbf{T},\ \boldsymbol{\mathcal{V}}_{\text{MONO}}(\mathbf{v}))$ is the orthogonal projection of $\mathbf{T}$ to the subspace $\boldsymbol{\mathcal{V}}_{\text{MONO}}(\mathbf{v})$ of elastic maps having a 2-fold axis in the direction $\mathbf{v}$. When feasible, we normally omit the superscript $\mathbf{T}$ in $\alpha^{\mathbf{T}}_{\text{MONO}}$.

Spherical plots of $\alpha_{\text{MONO}}(\mathbf{v})$ provide a powerful visualizaton tool for understanding elastic maps. Versions of these plots, which we refer to as α_{MONO}-spheres, have been used in François et al. (1998), Diner et al. (2010), and Tape & Tape (2022). A key feature of the α_{MONO}-sphere for $\mathbf{T}$ is its zero-valued contour, which consists of the directions where the material described by $\mathbf{T}$ has

2-fold symmetry axes; those axes determine the elasticity symmetry of the material. In particular, if the zero-contour is empty, then the material has only trivial symmetry.

α_{MONO}-spheres are complementary to the wave-velocity-based view of elastic maps, which displays how three Christoffel phase velocities (typically for P, fast-S, and slow-S) vary as a function of direction. α_{MONO}-spheres are better for determining elastic symmetry, while velocity spheres (Figure S2) are useful for interpreting traveltime-based measurements for low-anisotropy materials.

A fundamental tool in our study is the calculation of closest Σ-maps for a given map $\mathbf{T}$. They are given by

$$\mathbf{K}_\Sigma = \mathbf{K}_\Sigma^{\mathbf{T}} = \mathbf{P}\left(\mathbf{T},\, \boldsymbol{\mathcal{V}}_\Sigma(U_\Sigma^{\mathbf{T}})\right) \tag{4}$$

where Σ is one of the eight symmetry classes (TRIV, MONO, ..., ISO), $\mathbf{P}\left(\mathbf{T},\, \boldsymbol{\mathcal{V}}_\Sigma(U)\right)$ is the orthogonal projection of $\mathbf{T}$ onto the subspace $\boldsymbol{\mathcal{V}}_\Sigma(U)$ of Tape & Tape (2024, eq. 15), and $U_\Sigma^{\mathbf{T}}$ is a 3×3 rotation matrix that minimizes the angular distance function

$$\alpha_\Sigma^{\mathbf{T}}(U) = \angle\left(\mathbf{T}, \mathbf{P}\left(\mathbf{T},\, \boldsymbol{\mathcal{V}}_\Sigma(U)\right)\right) \tag{5}$$

over all rotation matrices U (Tape & Tape 2022).

The distance between two elastic maps $\mathbf{T}_A$ and $\mathbf{T}_B$ is $\|\mathbf{T}_B - \mathbf{T}_A\|$, and the angular distance is $\angle(\mathbf{T}_A,\, \mathbf{T}_B)$. We are especially interested in the angle between $\mathbf{T}$ and $\mathbf{K}_\Sigma$, the closest Σ-map to $\mathbf{T}$:

$$\beta_\Sigma = \beta_\Sigma^{\mathbf{T}} = \angle(\mathbf{T},\, \mathbf{K}_\Sigma^{\mathbf{T}}). \tag{6}$$

Our preferred measure of anisotropy is

$$\beta_{\text{ISO}} = \angle(\mathbf{T},\, \mathbf{K}_{\text{ISO}}). \tag{7}$$

The closest isotropic-map $\mathbf{K}_{\text{ISO}}$ is analytically determined from $\mathbf{T}$ (Appendix B) and therefore β_{ISO} is a simple calculation from the entries of the matrix for $\mathbf{T}$.

An approximate relationship between β_{ISO} and traditional measures of percent anisotropy AV appears to be $AV \approx 2\beta_{\text{ISO}}$, as shown in Figure S1 for the database of Brownlee et al. (2017).

2.1 An example

Figures 1 and 2 illustrate the concepts in the previous section. The example elastic map $\mathbf{T}$ we use is for a feldspar crystal reported by Brown et al. (2016), who concluded that the measured laboratory sample had triclinic (or trivial) symmetry.

Figure 1a displays the monoclinic angle function for $\mathbf{T}$, Figure 1b does the same for the closest MONO-map ($\mathbf{K}_{\text{MONO}}$) to $\mathbf{T}$, and Figure 1c does the same for the closest ORTH-map ($\mathbf{K}_{\text{ORTH}}$) to $\mathbf{T}$. Each of the elastic maps $\mathbf{K}_{\text{MONO}}$ and $\mathbf{K}_{\text{ORTH}}$ is obtained by performing a minimization over all rotation matrices U.

We plot green dots to depict the zero-contour, which provides a check in this example. Figure 1a has empty zero-contour and therefore exhibits no symmetry (i.e., trivial symmetry). Figure 1b has a zero-contour represented by the yellow arrow, representing a single 2-fold axis, which indicates MONO symmetry. Figure 1c has three perpendicular 2-fold axes represented by the colored arrows and coinciding green dots (6 total, 2 of which are visible); this represents ORTH symmetry.

Changing the viewpoint on the α_{MONO}-spheres helps show the 2-fold axes (or lack thereof). The colored axes in Figures 1a and 1b are the columns of the matrix $U_{\text{MONO}}^{\mathbf{T}}$ (i.e., $U_{\Sigma}^{\mathbf{T}}$ with $\Sigma = \text{MONO}$). The perspective for Figure 1d and Figure 1e is one that is looking down the third column of $U_{\text{MONO}}^{\mathbf{T}}$. From this perspective (or any other), we do not see 2-fold symmetry in Figure 1d. Moreover, the minimum value of the plotted function is $3.8°$ (light blue at center), which is greater than $0°$ and therefore not a 2-fold axis. By comparison, Figure 1e is monoclinic: it has a 2-fold symmetry axis (dark blue at center), and it has visible 2-fold symmetry.

The angular difference between the elastic maps $\mathbf{T}$ (Figure 1a) and $\mathbf{K}_{\text{MONO}}$ (Figure 1b) is $\beta_{\text{MONO}} = 3.8°$, which is the minimum value of the monoclinic angular distance function displayed on the α_{MONO}-sphere in Figure 1a. The 2-fold axis of $\mathbf{K}_{\text{MONO}}$ in Figure 1b is where the minimum value of $\alpha_{\text{MONO}}(\mathbf{v})$ occurs in Figure 1a.

Next we examine the higher-symmetry map of $\mathbf{K}_{\text{ORTH}}$ (Figure 1c). Figure 1f is the perspective looking down the yellow arrow ($\mathbf{u}_3$) in Figure 1c. The three 2-fold axes characteristic of orthorhombic symmetry are in the direction of the red, blue, and yellow arrows. The elastic map $\mathbf{K}_{\text{ORTH}}$ is $\beta_{\text{ORTH}} = 6.4°$ from $\mathbf{T}$.

We use the same elastic map $\mathbf{T}$, along with its closest ISO-map $\mathbf{K}_{\text{ISO}}$, to illustrate the notion of angles between elastic maps. The definition of β_Σ (Eq. 6) relates distance and angular distance. As illustrated in Figure 2a with $\Sigma = \text{ISO}$,

$$\sin \beta_{\text{ISO}} = d_{\text{ISO}} / \|\mathbf{T}\|. \tag{8}$$

In this example, $\|\mathbf{T}\| = 294.8$ GPa, $d_{\text{ISO}} = 129.4$ GPa, and $\beta_{\text{ISO}} = 26.0°$. The advantage of using β_{ISO} rather than d_{ISO} is that β_{ISO} does not depend on the size (or units) for $\mathbf{T}$. (In Figure 2, and elsewhere, the α_{MONO}-spheres for $\mathbf{K}_{\text{ISO}}$ are solid blue, because every direction is a 2-fold axis for $\mathbf{K}_{\text{ISO}}$, so that $\alpha_{\text{MONO}}^{\mathbf{K}_{\text{ISO}}}$ is identically zero.)

Figure 2b depicts the direct path from $\mathbf{T}$ to $\mathbf{K}_{\text{ISO}}$, which we will discuss in Section 4.2.

2.2 Lattice diagrams of elastic maps, Part I

The relationships among the eight symmetry classes can be depicted in a *lattice diagram* (François et al. 1998; Bóna et al. 2004; Tape & Tape 2022). We expand the lattice diagram concept by depicting an elastic map at each lattice node (or vertex) and by assigning the type—or mode (Section 4.5)—of the elastic map. An example is shown in Figure 3, which displays an α_{MONO}-sphere at each node in the lattice; we refer to these plots as a *lattice diagram of elastic maps*.

This representation, also displayed in Tape & Tape (2024), sets the stage for introducing several concepts. First, a lattice diagram conveys that there are eight elastic symmetry classes, as proven in various studies (Forte & Vianello 1996; Chadwick et al. 2001; Bóna et al. 2007; Tape & Tape 2021). Second, it provides a visual check on the α_{MONO}-sphere of the elastic map $\mathbf{S}_\Sigma$ displayed at each node: 1) Does it exhibit the intended symmetry, as conveyed by its zero contour? 2) Does it look somewhat similar to the α_{MONO}-sphere for the $\mathbf{T}$ map at the bottom? Third, the diagram offers a visual guide to the proximity of $\mathbf{T}$ to all the symmetry classes, which is a key question in many studies (see Section 3). While this assessment is quantified in terms of β_Σ (ideally with uncertainties), the α_{MONO}-spheres offer a more intuitive view. We will return to these diagrams in Section 4.1.

Fourth, the lattice diagram depicts the choice one has in reducing $\mathbf{T}$ toward a higher-symmetry map, as several model-parameter-space pathways toward $\mathbf{K}_{\text{ISO}}$ are possible, in addition to the direct path (Section 4.2). Lastly, there is a question of what type of map should be displayed at each lattice node (Section 4.5).

3 APPLICATIONS TO PREVIOUS STUDIES

Next we revisit four studies to illustrate how the approach in Section 2 can provide insights into elastic materials. Our emphasis is on calculating closest Σ-maps to the published results, and providing visualizations to guide interpretations of the elastic symmetry classes. The following examples in Sections 3.1 and 3.2 are based on measurements of common minerals and rocks: feldspars, amphiboles, granite, and gneiss. In Section 3.3 we examine the upper mantle elastic properties, as determined from ultramafic rocks and from a subduction flow model of the upper mantle.

3.1 Composition dependence of elastic symmetry

The study of Brown et al. (2016) estimated all 21 parameters, with uncertainties, of eight feldspar crystals having differing percentages of anorthite ranging from 0% (albite) to 96% (anorthite). The elastic map featured in Figures 1–3 is albite.

Figure 4a is a depiction of the symmetry of the eight feldspar maps in Table 2 of Brown et al. (2016). For each map $\mathbf{T}_i$ ($i = 1, \ldots, 8$) we calculate the closest Σ-map to $\mathbf{T}_i$ for seven Σ (MONO, ..., ISO). These 56 minimizations provide $\beta^i_\Sigma \equiv \beta^{\mathbf{T}^i}_\Sigma$, which are depicted by the dots in Figure 4a. To plot the uncertainty bars, we calculate 1000 realizations of each of the eight elastic maps using the published uncertainties in each C_{ij}. (Each map is generated in Voigt notation, then converted to $[\mathbf{T}]_{\mathbb{BB}}$.) In total, 56,000 minimizations were performed to make Figure 4a.

Figure 4a offers a compact view of the laboratory results from Brown et al. (2016). First, we can see that all feldspars exhibit clear trivial elastic symmetry, in that β^i_{MONO} are all above 0°, taking into account the $\pm 2\sigma$ uncertainties. Since all samples do not have monoclinic symmetry, they have only trivial symmetry. Second, β^i_{ISO} decreases from $26.0 \pm 0.4°$ for albite (An0) to $16.0 \pm 0.6°$ for anorthite (An96). Bulk modulus κ and shear modulus μ can be directly obtained from each $\mathbf{K}^{\mathbf{T}_i}_{\mathrm{ISO}}$ (Appendix B). Variations in κ and μ (Figure S6) reveal that the decrease in β^i_{ISO} with increasing anorthite percentage is due to an increase in κ, while μ remains stable. Interestingly, β_{MONO}, β_{ORTH}, and β_{TET} all increase for anorthite percentages increasing from 60% to 90%, suggesting some level of increasing anisotropy, even while β_{ISO} is decreasing.

Figure 4b provides a representation of the monoclinic elastic maps for nine amphibole crystals in Table 3 of Brown & Abramson (2016), shown with respect to their total aluminum content. The flat curve for $\beta_{\mathrm{MONO}} = 0°$ indicates that the elastic maps have monoclinic or higher symmetry. The values of $\beta_{\mathrm{ORTH}} = 2.5°$–$5.5°$ indicate that the amphiboles have monoclinic symmetry. The decreasing trend for all β_{Σ} curves indicates decreasing anisotropy with increasing aluminum content. For example, the two highest-aluminum samples decrease from $\beta_{\mathrm{ORTH}} = 4.3° \pm 0.2$ to $3.2° \pm 0.2$. By comparison, the trends in C_{ij} do not exhibit this: Brown & Abramson (2016) noted, "Five moduli (C_{33} C_{23} and the monoclinic moduli C_{15} C_{25} and C_{35}) have no significant dependence on aluminum." The aluminum replacement of cations—Si in plagioclase, Si and Mg/Fe in amphiboles—results in small changes in bond lengths and angles. This corresponds with decreasing anisotropy (β_{ISO}: Figure 4b), though a causal connection between the crystallographic change and the elasticity change remains unclear.

3.2 Pressure and temperature dependence of elastic symmetry

Figure 5 is a compilation of results from two studies that examined the dependence of elasticity on pressure and temperature for granite and gneiss (Lokajíček et al. 2021; Aminzadeh et al. 2022). Lokajíček et al. (2021) examined Westerly (Rhode Island, USA) granite and inferred orthorhombic elastic symmetry at low pressures. For the WG100 0.1 MPa elastic map in their Table 3, we calculate values of $\beta_{\mathrm{MONO}} = 0.4°$, $\beta_{\mathrm{ORTH}} = 0.5°$, and $\beta_{\mathrm{TET}} = 1.6°$. Assuming error-free measurements, one would conclude that the material has trivial symmetry, since $\beta_{\mathrm{MONO}} > 0°$. However, allowing for uncertainties in measurements, one might adopt an uncertainty in β of, say, $\pm 0.5°$, which would imply that that material has orthorhombic symmetry ($\beta_{\text{ORTH}} = 0.5° \pm 0.5$) but not tetragonal symmetry ($\beta_{\text{TET}} = 1.6° \pm 0.5$). Uncertainty estimates would be needed to better determine the symmetry.

Figure 5a provides visual support for the findings in Lokajíček et al. (2021): "…increase of preheating temperature enhances the anisotropy…" Figure 5b and c convey the results from Aminzadeh et al. (2022) who examined how elasticity is influenced by changing pressure for two rock samples: Grimsel granite (b) and Bukov gneiss (c). The figures directly support the author's conclusions: "While the Grimsel granite is very sensitive to pressure and becomes almost isotropic at high pressures, a great portion of anisotropy in the Bukov migmatized gneiss remains even under high pressures due to its texture." In terms of Figure 5b and c, at 100 MPa, the Grimsel granite has $\beta_{\text{ISO}} = 2.3°$ while the Bukov gneiss has $\beta_{\text{ISO}} = 6.2°$.

Aminzadeh et al. (2022) state: "We demonstrate that the Bukov migmatized gneiss is orthorhombic, whereas the Grimsel granite is transversely isotropic under atmospheric pressure." The leftmost dots in Figure 5b and c, for atmospheric pressure (0.1 MPa), would lead to a different assessment. Both samples have very similar β_Σ values to each other for MONO, ORTH, TET, TRIG, and XISO, so any assignment of symmetry would be expected to be the same. Furthermore, any assignment would depend on uncertainties in C_{ij}, which were not available. As displayed in Figure 5b and c, both samples have trivial elastic symmetry at 0.1 MPa, since $\beta_{\text{MONO}} > 2°$.

3.3 Rocks and subduction flow models for the upper mantle

We revisit two studies focusing on the upper mantle that include rock measurements (Ji et al. 1994) and crytallographic preferred orientation (CPO) anisotropy estimates for olivine from global mantle flow models (Becker et al. 2008). Ji et al. (1994) performed petrofabric analyses of ultramafic xenolith samples from three localities of northwestern North America: Castle Rock (CR), Alligator Lake (AL), and Nunivak Island (NI). For each locality, they determined an average elastic map based on 4-5 samples. Examining the seismic velocity patterns expected for these elastic maps, the authors noted "remarkably similar seismic properties" and also "quasi-orthorhombic geometry".

These inferences can be quantified with β_Σ angles and with lattice diagrams (e.g., Figure 3), which are provided in Tape & Gupta (2024). The β_{ORTH} angles are $0.2°$ (CR), $0.2°$ (AL), and $0.2°$ (NI), while the β_{XISO} angles are $0.7°$ (CR), $0.6°$ (AL), and $1.4°$ (NI). Lacking uncertainties on the published C_{ij} entries, we cannot determine the uncertainties in β_Σ that would be needed to assign a symmetry to each elastic map. If we adopt a threshold of $0.5°$ for this assignment, then we would assign ORTH to all three maps. If instead we adopted a threshold of $1°$, we would assign XISO to CR and AL and ORTH to NI.

Mantle flow models can be used to infer three-dimensional variations in elasticity in the Earth's mantle (Gaboret et al. 2003; Becker et al. 2003, 2006; Behn et al. 2004; Walker et al. 2011). Although global estimates of olivine CPO from flow provide all 21 elastic parameters, the elastic maps are not strongly anisotropic ($\beta_{\text{ISO}} < 5°$) and are often approximated as XISO in order to visualize 3D variations in the elastic maps (Becker et al. 2006; VanderBeek & Faccenda 2021).

Our approach provides an answer to the question, What is the global distribution of elastic symmetry for a given 3D model? Two subtle decisions are required. First, a node sequence (Section 4.6) needs to be assumed, since this specifies what is meant by a higher or lower symmetry class. Second, if no uncertainties are provided for the published C_{ij}, then there are no uncertainties for β_Σ, and therefore we need to choose a threshold value β_{trsh}.

To illustrate our approach, we use a global model of elasticity at 200 km depth from Becker et al. (2008) (see Data Availability for link to data set). We choose the node sequence TRIV-MONO-ORTH-TET-XISO-ISO. Let $\mathbf{T}(\mathbf{r})$ represent one of the 14,512 elastic maps for direction $\mathbf{r}$ on Earth. For each $\mathbf{T}(\mathbf{r})$, we perform four minimizations to obtain the closest Σ-maps and their corresponding $\beta_{\text{MONO}}(\mathbf{r})$, $\beta_{\text{ORTH}}(\mathbf{r})$, $\beta_{\text{TET}}(\mathbf{r})$, and $\beta_{\text{XISO}}(\mathbf{r})$; $\mathbf{K}_{\text{ISO}}$ and $\beta_{\text{ISO}}(\mathbf{r})$ are determined analytically. An example global plot, for β_{XISO}, is shown in Figure 6a, with others in Figure S7.

From a set of β_Σ global plots, we determine a *spatial sigma plot*, which assigns the elastic symmetry $\Sigma(\mathbf{r})$ for each spatial location $\mathbf{r}$. This is achieved by starting with β_{MONO} for a given elastic map $\mathbf{T}$. If $\beta_{\text{MONO}} > \beta_{\text{trsh}}$, then $\mathbf{T}$ is assigned TRIV. If $\beta_{\text{MONO}} \leq \beta_{\text{trsh}}$, then $\mathbf{T}$ has MONO or higher symmetry and we check if $\beta_{\text{ORTH}} > \beta_{\text{trsh}}$; if it is, then we assign $\mathbf{T}$ MONO symmetry. If $\beta_{\text{ORTH}} \leq \beta_{\text{trsh}}$, then $\mathbf{T}$ has ORTH or higher symmetry. This procedure is continued to TET, XISO, and ISO, until each $\mathbf{T}$ is assigned a Σ.

For the chosen node sequence and a chosen threshold of $\beta_{\rm trsh} = 1.0°$, the resulting spatial sigma plot is shown in Figure 6b, where 66.9% of the global points are assigned XISO, 23.1% ORTH, 8.5% ISO, and the remaining 1.5% TET or MONO. These percentages are strongly dependent on $\beta_{\rm trsh}$, and ideally no choice would be needed if uncertainties in C_{ij} (including covariances) were provided. Further analysis could explore the correspondence between ORTH regions and the age of oceanic plates, as well as the directional variations of the XISO symmetry axes (Figure S8), with near-vertical axes expressing VTI symmetry and near-horizontal axes expressing HTI symmetry.

4 NAVIGATION WITHIN THE SPACE OF ELASTIC MAPS

A laboratory experiment will collect a large number of measurements for an elastic material, with the goal of determining the set of 21 parameters of the matrix of the elastic map $\mathbf{T}_0$ that best fits the measurements. It may also be desirable to consider alternatives to $\mathbf{T}_0$ by favoring elastic maps that either have higher symmetry (e.g., TET instead of TRIV) or lower anisotropy (lower value of $\beta_{\rm ISO}$). For these pursuits, we introduce a framework for navigating the 21-dimensional space of elastic maps. Our approach includes a combination of terminology and visualization. We will introduce several concepts and then illustrate them in figures. All examples are based on the feldspar elastic map introduced in Figure 1.

4.1 Lattice diagrams of elastic maps, Part II

A symmetry of a material is a rotation of the material that leaves its elastic map unchanged. The symmetry group of the material is the group of all such rotations. The 2-fold points of the group are the points where the 2-fold axes of the group intersect the unit sphere.

The symmetry class of the material, informally, is its symmetry group but without its orientation information. Tape & Tape (2022, Section 2.8) has a precise definition of symmetry class, including an illustration.

Figure 7a is an abridged version of the lattice diagram in Figure 3. For each Σ, all but the zero-contour has been removed from the contour plot of $\alpha^{\mathbf{K}_\Sigma}_{\rm MONO}$ in Figure 3. Since the zero-contour (blue) consists of the 2-fold points of the symmetry group of $\mathbf{K}_\Sigma$, and since the 2-fold points determine the group, then the lattice in Figure 7a is a depiction of the symmetry group of $\mathbf{K}_\Sigma$ for each Σ.

The figure expresses a partial ordering of symmetry classes: For two nodes connected by an upward-trending path in the figure, the Σ class at the upper node has "higher symmetry" than that at the lower node. Thus each of $\Sigma = \text{XISO}, \text{CUBE}, \text{ISO}$ is higher symmetry than TRIG, but neither of TRIG and ORTH is higher than the other.

In general, each elastic symmetry group is determined by a rotation matrix U and one of the eight Σ. The choice of Σ determines the unoriented configuration of 2-fold points for the group, and U orients the configuration. Figure 7b shows the unoriented configuration for each Σ. The groups are the elastic symmetry "reference groups", one for each Σ. For each Σ, the rotation U_Σ in Figure 7a rotates the blue points at the Σ node in Figure 7b to the blue points at the Σ node in Figure 7a. For $\Sigma = \text{TET}$, for example, U_Σ appears to be approximately a $90°$ rotation about the y-axis.

The solid paths in the lattices indicate inclusions among the reference groups. They can be confirmed just by examining the blue dots in Figure 7b. Thus, for example, the TRIG reference group is contained in the XISO reference group (recognizing that the 3-fold TRIG axis aligns with the N-fold XISO axis), but not in the CUBE reference group, even though CUBE symmetry is higher than TRIG symmetry.

In Section 2.2 we introduced lattice diagrams for the purpose of displaying the set of closest Σ-maps to $\mathbf{T}$. The diagrams serve an additional purpose of depicting the choices one has in reducing $\mathbf{T}$ toward a higher-symmetry map, as several pathways toward $\mathbf{K}_{\text{ISO}}$ are possible, in addition to the direct path from $\mathbf{T}$ to $\mathbf{K}_{\text{ISO}}$ (Section 4.2). Furthermore, there is a question of what type of elastic map should occupy each lattice node (Section 4.5).

4.2 Direct path between two elastic maps

The *direct path* from elastic map $\mathbf{T}_A$ to elastic map $\mathbf{T}_B$ is parameterized by

$$\mathbf{T}_A^B(t) = (1-t)\,\mathbf{T}_A + t\,\mathbf{T}_B. \tag{9}$$

For example, a map between $\mathbf{T}$ and its closest isotropic map $\mathbf{K}_{\text{ISO}}$ is

$$\mathbf{T}(t) = \mathbf{T}_{\mathbf{T}}^{\mathbf{K}_{\text{ISO}}}(t) = (1-t)\,\mathbf{T} + t\,\mathbf{K}_{\text{ISO}} \tag{10}$$

Figure 2b shows elastic maps $\mathbf{T}(t)$ for four values of t. As t increases from 0 to 1, the map $\mathbf{T}(t)$ transitions from $\mathbf{T}$ to $\mathbf{K}_{\text{ISO}}$, while β_{ISO} decreases from $26.0°$ to $0°$.

4.3 Base maps

We refer to an ordered set of elastic maps $\mathbf{T}_i$ as *base maps*, with i being an index. One example of a set of base maps is the direct path. For example, using Equation (10) with $t_i \in [0, 1]$ and discretized in 0.2 spacing, we obtain six maps $\mathbf{T}_i = \mathbf{T}(t_i)$ that vary from $\mathbf{T}_A$ ($t_1 = 0$) to $\mathbf{T}_B$ ($t_6 = 1$). The set of base maps forms a *pathway*. The term *base* is chosen because these maps can be thought of as forming the base of beta curves, described next.

4.4 Beta curves

For any map $\mathbf{T}$ and any Σ we can calculate the closest Σ map $\mathbf{K}_{\Sigma}^{\mathbf{T}}$ to $\mathbf{T}$ and consider its angular distance β_{Σ} from $\mathbf{T}$ (Eq. 6). A *beta curve* depicts a set of β_{Σ} for an ordered set of elastic maps.

Figure 8 provides an example of seven beta curves for the direct path from $\mathbf{T}$ to $\mathbf{K}_{\text{ISO}}$, represented in Equation (10) and discretized as before. For each of the six maps $\mathbf{T}_i = \mathbf{T}(t_i)$ ($t_i = 0, 0.2, \ldots, 1.0$) and for each Σ, we calculate a closest Σ-map $\mathbf{K}_{\Sigma}^{\mathbf{T}_i}$ and its corresponding $\beta_{\Sigma}^{\mathbf{T}_i}$. This results in the seven beta curves in Figure 8, which conveys two main points. First, the first five maps $\mathbf{T}_i$ have trivial symmetry, as exhibited by $\beta_{\text{MONO}}^{\mathbf{T}_i} > 0$. Second, for increasing t, the beta curves decrease steadily to zero. The $t = 1$ elastic map is $\mathbf{K}_{\text{ISO}}$, which has ISO symmetry and therefore also all other symmetries, which is why all the β_{Σ} curves decrease to $0°$. Lastly, note that negative values of t allow for elastic maps that are more anisotropic than $\mathbf{T}$ (i.e., farther from isotropic) while having the same closest ISO map. For the BrownAn0 elastic map, $\beta_{\text{ISO}} = 26.0°$ for $t = 0$ (see Figure 3), and negative values of t produce much more anisotropic elastic maps, all the way to $t = -0.66$, for which $\beta_{\text{ISO}} = 39.0°$. For $t \leq -0.67$, the elastic map $\mathbf{T}(t)$ has a negative eigenvalue and is therefore unphysical.

Figure 9 illustrates the direct path of elastic maps by displaying (a) α_{MONO}-spheres and (b) synthetic seismograms computed for homogeneous media having these properties (see Appendix C). Empirically, for elastic map $\mathbf{T}$, the maximum value of its α_{MONO}-sphere is strongly correlated with its β_{ISO}, so from inspection of the six α_{MONO}-spheres, we can infer from the red colors of $\mathbf{T}$ ($t = 0$) that it has the highest level of anisotropy among the displayed spheres. Towards $t = 1$ ($\mathbf{K}_{\mathrm{ISO}}$), the α_{MONO}-spheres grade to uniform blue, representing isotropy. The changes in seismograms are dramatic though (Figure 9): for the isotropic case ($t = 1$: top), we see only a P wave and S wave, as expected. For all other cases, we see more than two arrivals, and we do not see a smooth transition in seismograms for varying t, as we did in the case of the α_{MONO}-spheres. The types of phases, the arrival times, and the amplitudes all change significantly for each elastic map. This reveals that linear changes in anisotropy (here, parameterized by t) can result in nonlinear changes in the seismic waveforms, even for a homogeneous material. By comparison, in classical travel-time tomography, a linear change in slowness ($1/V$) results in a linear change in arrival time (Liu & Gu 2012). The occurrence of more than three waveform arrivals for a homogeneous material (Figure 9) is consistent with theoretical predictions from Christoffel group (not phase) velocities (Červený 2001), as shown in Figures S10 and S11 and as demonstrated in previous studies (Igel et al. 1995; Komatitsch et al. 2000).

4.5 Node modes

The *node mode* describes how the elastic maps are determined at the nodes of the lattice diagram. We introduce three different node modes. For each mode the elastic map $\mathbf{S}_\Sigma$ at the lattice node Σ is the orthogonal projection of $\mathbf{T}$ onto the Σ subspace $\boldsymbol{\mathcal{V}}_\Sigma(U)$ (Tape & Tape 2024, eq. 15). The node mode determines U as follows: For node mode 1, U is chosen by the user and is the same for all Σ. For node mode 2 the matrix U is $U_\Sigma^{\mathbf{T}}$ as described in connection with Equation (5). The elastic map $\mathbf{S}_\Sigma$ is therefore the closest Σ-map to $\mathbf{T}$. For node mode 3, the elastic map $\mathbf{S}_\Sigma$ is the closest Σ-map to the previous map within a particular node sequence. Our main results feature node mode 2, and we provide additional comparisons with node modes 1 and 3 in Figures S3–S4.

4.6 Node sequences

A *node sequence* is a special pathway. It is a sequence of elastic maps defined on the nodes of a lattice and having the same node mode. Of particular interest are the four sequences between TRIV and ISO that follow increasing symmetry: TRIV-MONO-ORTH-TET-XISO-ISO, TRIV-MONO-ORTH-TET-CUBE-ISO, TRIV-MONO-TRIG-CUBE-ISO, and TRIV-MONO-TRIG-XISO-ISO. Removing any of the nodes within these four node sequences results in a new node sequence. For example, ORTH-XISO-ISO and TRIV-MONO-ISO are node sequences. Technically, the direct paths such as TRIV-ISO or MONO-ORTHare also node sequences.

4.7 Cumulative internodal angle curves

A *cumulative internodal angle curve*, which we will shorten to *cumulative curves*, is a sum of internodal angles for a given node sequence and node mode in a lattice. It provides a measure of the angular distance traversed by the node sequence, and it can be compared with the direct-path distance between the first and last node in the sequence.

Figure 10a displays a cumulative curve for an example node sequence and node mode. The direct path from $\mathbf{T}$ to $\mathbf{K}_{\text{ISO}}$ is $26.0°$, while the cumulative angular distance through the node sequence is $50.3°$. The matrix of internodal angles in Figure 10b conveys the possible pathways for a given node sequence, as described next. The default path for the cumulative curve is the one that passes through all listed symmetry classes; the internodal angles follow the first off-diagonal and have values of $3.8°$ (TRIV-MONO), $5.2°$ (MONO-ORTH), $4.8°$ (ORTH-TET), $17.9°$ (TET-XISO), and $18.5°$ (XISO-ISO), resulting in a cumulative angular distance of $50.3°$. Intermediate nodes can be omitted, resulting in a different node sequence and a different cumulative distance. If all four intermediate nodes are omitted, then the node sequence becomes the direct path from TRIV to ISO, represented by the upper right entry in Figure 10b ($26.0°$).

Given a TRIV elastic map estimated from measurements, it may be desirable to bias the estimation procedure toward an elastic map having lower anisotropy (smaller β_{ISO}) or a map having higher symmetry than TRIV. This distinction is a choice between the direct path and a node sequence having at least three nodes. The direct path is the shortest, and all intermediate maps between $\mathbf{T}$ and $\mathbf{K}_{\text{ISO}}$ have TRIV symmetry. The node sequence is a longer path (Figure 10a) and includes maps having higher symmetry. A longer path will generally involve a greater exploration of model parameter space and be associated with increased computational cost. This choice illustrates the tradeoff between seeking higher-symmetry possibilities at the expense of a longer pathway. We revisit this topic of regularization in Section 5.

4.8 Visual guide to navigating the space of elastic maps

We are now equipped to review a full set of figures (Figures 3 and 8–12) which use the BrownAn0 map as an example. Figure 3 features node mode 2, meaning that the maps at each lattice node are a closest Σ-map to $\mathbf{T}$, denoted $\mathbf{K}_{\Sigma}$ or $\mathbf{K}_{\Sigma}^{\mathbf{T}}$. This means that the orientation U_{Σ} for each $\mathbf{K}_{\Sigma}$ may be very different, as shown by the set of tri-colored axes in Figure 3. For example, from inspection of the α_{MONO}-spheres (and U-axes) of $\mathbf{K}_{\text{XISO}}$ and $\mathbf{K}_{\text{TET}}$, we see that the 4-fold TET axis (yellow arrow) is not aligned with the N-fold XISO axis (yellow arrow).

With the given node mode and $\mathbf{T}$ in Figure 3, there are multiple paths—node sequences—from $\mathbf{T}$ to $\mathbf{K}_{\text{ISO}}$, one of which is TRIV-MONO-ORTH-TET-XISO-ISO and featured in Figure 10a. Between any pair of lattice nodes we can discretize a path using Equation (9). For example, the 11 maps displayed in Figure 11 include the nodes TRIV-MONO-ORTH-TET-XISO-ISO, as well as one additional elastic map between each pair of nodes. The seismogram differences—notably between $\mathbf{T}$ and $\mathbf{K}_{\text{MONO}}$—imply that, given suitable coverage of seismic stations, it should be possible to use recordings to estimate the full elastic map (i.e., 21 parameters) for a relatively homogeneous material. The estimation problem would require having volumetric sensitivities of seismic waveform differences for each of the 21 parameters; components of this procedure can be found in Sieminski et al. (2007), Köhn et al. (2015), and Beller & Chevrot (2020).

The beta curves in Figure 12 are constructed starting with a choice of node mode and node sequence. The node sequence contains six of the eight elastic maps in Figure 3. As it turns out, beta curves are generally nonlinear between nodes and therefore we need more maps than the nodes in order to show how symmetry varies along the path. In Figure 12, we use four maps between each pair of adjacent nodes in the sequence, resulting in a total of 26 maps from $\mathbf{T}$ to $\mathbf{K}_{\text{ISO}}$.

The beta curves in Figure 12 depend on the elastic map $\mathbf{T}$ and on the choices of node sequence, node mode, and discretization interval between nodes. In many investigations, a material measured to have TRIV symmetry will be assumed to have higher symmetry. Analogs of Figure 12, perhaps with other choices of node sequence, node mode, and discretization interval, may provide a more informed and less arbitrary basis for assigning a particular symmetry to the material.

5 DISCUSSION

5.1 Laboratory measurements of minerals and rocks

Any laboratory experiment seeking to estimate the 21 elastic parameters for a homogeneous material is apt to obtain an elastic map that has trivial symmetry, no matter what the material is. Even a single crystal such as garnet, which might be expected to have cubic elastic symmetry (Jiang et al. 2004; Almqvist & Mainprice 2017), would have trivial symmetry if all 21 parameters were estimated and if uncertainties were not considered. This leads to two future-looking points. First, it is helpful to perform measurements that enable the estimation of as many elastic parameters as possible. Second, no matter how many elastic parameters are listed, they should ideally be accompanied by uncertainties.

Compilations of elastic parameters contain assumptions about the materials. For example, the expansive Table 2 of Almqvist & Mainprice (2017) categorizes materials by crystal system, and almost all materials are represented with a subset of 21 C_{ij} values. However, the link between crystallographic symmetry and elastic symmetry is tenuous, as articulated by Forte & Vianello (1996). For example, even though a garnet has cubic crystallographic symmetry, it would be preferable to estimate as many C_{ij} as possible, rather than assume cubic elastic symmetry and list only three unique C_{ij}.

There are few studies listing 21 elastic parameters and fewer that also list uncertainties. Almqvist & Mainprice (2017) listed two studies: Militzer et al. (2011) and Brown et al. (2016). Vestrum et al. (1996) and Brown et al. (2016) listed uncertainties for all 21 parameters. Uncertainty estimates are especially important for assessing the elastic symmetry class of a material, as we saw in Section 3.2 for the granite and gneiss samples analyzed by Aminzadeh et al. (2022). Looking toward the future, it should be possible to estimate covariances among the 21 elastic parameters, leading to a 6×6 data covariance matrix $\mathbf{C}_{\mathrm{D}}$. This would improve the error propagation procedures in calculating quantities such as the uncertainties in β_Σ angles (e.g., Figure 4), which are needed to infer the elastic symmetry of a material.

5.2 Estimation at the laboratory scale

Elastic parameters are estimated from laboratory measurements (Angel et al. 2009). For the sake of discussion, we will represent the parameter estimation problem with the function

$$f(\mathbf{T}) = \|\mathbf{g}(\mathbf{T}) - \mathbf{d}\|, \tag{11}$$

where $\mathbf{d}$ is a set of three-component seismograms from receivers surrounding the material for a given set of sources, and $\mathbf{g}(\mathbf{T})$ is the corresponding set of synthetic seismograms for the same sources and receivers, given an elastic map $\mathbf{T}$. We seek the $\mathbf{T}$ that minimizes $f(\mathbf{T})$.

Let's assume we have estimated 21 T_{ij} for a material. From the estimated $\mathbf{T}_0$, we can calculate closest Σ maps ($\mathbf{K}_\Sigma$), along with their corresponding β_Σ angles. For example, β_{ISO} provides a measure of overall anisotropy, while $\beta_{\mathrm{MONO}} > 0^\circ$ would indicate trivial elastic symmetry. We may wish to bias our estimated $\mathbf{T}_0$ toward having either lower anisotropy (lower β_{ISO}) or higher-symmetry representations (MONO, ORTH, etc). This biased elastic map will be denoted by $\mathbf{T}_k$. Next we discuss four possibilities for obtaining $\mathbf{T}_k$; some of these are already undertaken with laboratory data, while others are an opportunity for future research.

First, we can consider distinct pathways between $\mathbf{T}_0$ and $\mathbf{K}_{\mathrm{ISO}}$, such as the direct path or a path that traverses a sequence of nodes to the closest isotropic map (Section 4). We can then directly evaluate the waveform misfit $f(\mathbf{T})$ for all the elastic maps along this pathway. Assuming that $\mathbf{T}_0$ is the global best-fitting elastic map, then all other maps—including along the pathway—will have higher misfit with recorded waveforms. Nevertheless, they may be more desirable for interpretation purposes, especially when considering uncertainties in T_{ij}.

A second approach is to re-estimate T_{ij} for a fixed symmetry class. For example, restrict the estimation problem by constraining $\mathbf{T}$ to have MONO, ORTH, ..., ISO elastic symmetry. This would produce a set of best-fitting maps, with higher misfit expected for higher-symmetry (lower-parameter) Σ.

A third approach is to estimate T_{ij} using a modified misfit function (see Eq. 11)

$$f_{\Sigma k}(\mathbf{T}) = \|g(\mathbf{T}) - \mathbf{d}\| + k\beta_{\Sigma}^{\mathbf{T}} \tag{12}$$

where $k \geq 0$ is a user-chosen weight and Σ is a user-chosen symmetry class. This will result in a TRIV $\mathbf{T}_k$ that is close to having Σ (or higher) elastic symmetry while also producing higher misfits with observations ($f(\mathbf{T}_k) > f(\mathbf{T}_0)$). For example, rather than allowing only ORTH elastic symmetry, as in the second approach, one could bias (trivial) $\mathbf{T}$ toward ORTH symmetry by minimizing Equation (12).

A fourth approach is a special case of the third approach: choose $\Sigma = \text{ISO}$ and estimate T_{ij}. This is perhaps the most natural and efficient approach, since β_{ISO} represents the magnitude of anisotropy and since it is analytical (Appendix B) and does not require numerical minimization. Choices of large k will bias $\mathbf{T}_k$ toward more isotropic materials, while $k = 0$ would result in $\mathbf{T}_0$ via Equation (11).

5.3 Prospects for seismic imaging

Seismic imaging of Earth's interior brings three compounding challenges: 1) sparse, irregular station coverage at the surface; 2) strong heterogeneity in the form of varying material properties with space and also varying complexity of interfaces between materials (such as the topographic surface); and 3) the presence of anisotropic materials at a large range of scales. We focus on two forms of complexity: spatial heterogeneity and materials with up to 21 elastic parameters.

These two complexities are typically handled with two forms of regularization. The first is to impose a constraint on the estimation problem, by penalizing models that exhibit strong spatial variations in elastic properties. This can also be achieved by modifying the misfit function or by assuming coarse cells in the volume, which guarantee uniform properties across portions of the estimated subsurface model.

The second form of regularization is to impose a constraint on the elastic symmetry (approach 2 in Section 5.2), which is the current practice in seismic tomography. The most common choices are isotropy (e.g., V_{P} and V_{S}) and transverse isotropy. Transverse isotropy is defined by 7 parameters in general (TTI: tilted transverse isotropy), 6 parameters if the (main, i.e., regular) symmetry axis is horizontal (HTI: horizontal transverse isotropy), and 5 parameters if the symmetry axis is vertical (VTI: vertical transverse isotropy). In these cases, the 21-D model parameter space is massively reduced by the choice of XISO symmetry class and then further reduced by restrictions on the orientation of the XISO axis. (Analogous reductions for other symmetries can be obtained by imposing restrictions on U_{Σ}.)

An alternative is to incorporate a penalty function into the misfit function, such as in Eq. 12, where minimization will favor spatial models with 21-parameter materials having lower anisotropy (lower β_{Σ}). With a large choice of k and with $\Sigma = \textsc{iso}$, the estimation problem will produce a nearly-isotropic model that best fits the data: in other words, a traditional V_{P} and V_{S} tomography approach. Further work is needed to explore the application of the framework presented in Section 4 to seismic imaging.

Finally, we acknowledge that the distinction between laboratory and field scales is also one of length scale of seismic waves that are probing the materials. For example, a 5-cm rock sample in Section 3.2 may appear homogeneous to certain low-frequency (long-wavelength) waves, while exhibiting extreme heterogenitiy to high-frequency waves. Characterization of elastic properties is inherently scale-dependent, a topic in the realm of homogenization (Capdeville et al. 2010).

6 CONCLUSION

Materials measured in the lab are apt to exhibit trivial elastic symmetry, with all 21 parameters needed in order to fit the measurements. In some cases, the estimated uncertainties of elastic parameters will demonstrate that the material—say, a feldspar crystal—indeed has trivial elastic symmetry. In other cases, the uncertainties will indicate that higher-symmetry representations—

perhaps even isotropic—are possible. We provide strategies for understanding elastic maps, as well as their possible reductions toward lower-parameter (higher-symmetry) or lower-anisotropy versions. The demonstrations in Section 3 suggest that additional insights may be gained with modest effort.

It remains to be seen how seismic imaging problems—where data coverage is sparse and heterogenity is high—can be generalized to consider 21-parameter materials while accommodating regularization favoring isotropic elastic maps. If a 21-dimensional model parameter space seems daunting for a homogeneous material in the lab, a heterogenous subsurface region may seem impossible (and even unsensible) to characterize in terms of its spatial variations. Nevertheless, there is value in considering these extreme possibilities and establishing strategies that can be employed to handle measurement uncertainties, quantify model uncertainties, and incorporate prior information (or bias) in the estimation problem. The framework in Sections 2 and 4 helps one operate within—and comprehend—the 21-dimensional space of elastic maps, which is an essential component of the pursuit to characterize Earth materials.

ACKNOWLEDGMENTS

We thank an anonymous reviewer and Josh Russell for providing detailed, constructive feedback on the manuscript. A. Gupta and C. Tape were supported by National Science Foundation grant EAR 2342129. We thank Daniel Peter for maintaining Specfem3D software, including capabilities for anisotropic wave propagation. Specfem3D is part of the SCOPED project, which is supported by grant OAC 2104052 from the National Science Foundation. Seismic wavefield simulations were done on the high-performance computing cluster at the UAF Geophysical Institute's Research Computing Systems. We thank Walt Tape, Jeroen Tromp, Qinya Liu, and Nanqiao Du for helpful discussions. Nanqiao Du provided the code to calculate Christoffel group velocities used in Figures S10 and S11. For assistance in writing codes in Python and Mathematica, we used AI tools based on GPT models. PyGMT (v0.13.0; Tian et al. 2024; Wessel et al. 2019) was used to plot Figure 6.

DATA AVAILABILITY

The elastic maps featured in Section 3 are available from the cited publications. The global set of elastic maps featured in Figure 6 is available at `https://www-udc.ig.utexas.edu/external/becker/anisotropy_model.html`. The database of elastic maps of Brownlee et al. (2017) (Figure S1) was provided to C. Tape by S. Brownlee.

Calculations and figures were done using open-source software in Python (`https://github.com/uafgeotools/elasticmapper`) and using Mathematica (`https://community.wolfram.com/groups/-/m/t/3180725` and `https://github.com/carltape/mtbeach`). Details and examples of lattice diagrams like Figure 3 are available in Tape & Gupta (2024) for 28 example elastic maps. A large set of synthetic seismograms, including the ones displayed in Figures 9 and 11, is available in Gupta (2025).

SUPPLEMENTARY MATERIAL

Table S1, Figures S1–S11, and accompanying text.

REFERENCES

Abt, D. L., Fischer, K. M., Abers, G. A., Strauch, W., Protti, J. M., & González, V., 2009. Shear wave anisotropy beneath Nicaragua and Costa Rica: Implications for flow in the mantle wedge, *Geochem. Geophy. Geosyst.*, **10**(5).

Alkhalifah, T. & Plessix, R.-E., 2014. A recipe for practical full-waveform inversion in anisotropic media: An analytical parameter resolution study, *Geophysics*, **79**(3), 91–101.

Almqvist, B. S. G. & Mainprice, D., 2017. Seismic properties and anisotropy of the continental crust: Predictions based on mineral texture and rock microstructure, *Rev. Geophys.*, **55**, 367–433.

Aminzadeh, A., Petružálek, M., Vavryčuk, V., Ivankina, T. I., Svitek, T., Petrlíková, A., Staš, L., & Lokajíček, T., 2022. Identification of higher symmetry in triclinic stiffness tensor: Application to high pressure dependence of elastic anisotropy in deep underground structures, *International Journal of Rock Mechanics & Mining Sciences*, **158**, 1–16.

Angel, R. J., Jackson, J. M., Reichmann, H. J., & Speziale, S., 2009. Elasticity measurements on minerals: a review, *European J. Mineraology*, **21**, 525–550.

Backus, G. E., 1962. Long-wave elastic anisotropy produced by horizontal layering, *J. Geophys. Res.*, **67**(11), 4427–4440.

Bakulin, A., Woodward, M., Nichols, D., Osypov, K., & Zdraveva, O., 2010. Building tilted transversely isotropic depth models using localized anisotropic tomography with well information, *Geophysics*, **75**(4), 27–36.

Becker, T. W., Kellogg, J. B., Ekström, G., & O'Connell, R. J., 2003. Comparison of azimuthal seismic anisotropy from surface waves and finite-strain from global mantle-circulation models, *Geophys. J. Int.*, **155**, 696–714.

Becker, T. W., Chevrot, S., Schulte-Pelkum, V., & Blackman, D. K., 2006. Statistical properties of seismic anisotropy predicted by upper mantle geodynamic models, *J. Geophys. Res.*, **111**, 1–16.

Becker, T. W., Kustowski, B., & Ekström, G., 2008. Radial seismic anisotropy as a constraint for upper mantle rheology, *Earth Planet. Sci. Lett.*, **267**, 213–227.

Behn, M. D., Conrad, C. P., & Silver, P. G., 2004. Detection of upper mantle flow associated with the African Superplume, *Earth Planet. Sci. Lett.*, **224**, 259–274.

Beller, S. & Chevrot, S., 2020. Probing depth and lateral variations of upper-mantle seismic anisotropy from full-waveform inversion of teleseismic body-waves, *Geophys. J. Int.*, **222**, 352–387.

Birch, F., 1961. The velocity of compressional waves in rocks to 10 kilobars, Part 2, *J. Geophys. Res.*, **66**(7), 2199–2224.

Bóna, A., Bucataru, I., & Slawinski, M. A., 2004. Material symmetries of elastic tensors, *Q. J. Mechanics and Applied Mathematics*, **57**(4), 583–598.

Bóna, A., Bucataru, I., & Slawinski, M. A., 2007. Coordinate-free characterization of the symmetry classes of elastic tensors, *J Elasticity*, **87**, 109–132.

Brown, J. M. & Abramson, E. A., 2016. Elasticity of calcium and calcium-sodium amphiboles, *Phys. Earth Planet. Inter.*, **261**, 161–171.

Brown, J. M., Angel, R. J., & Ross, N. L., 2016. Elasticity of plagioclase feldspars, *J. Geophys. Res. Solid Earth*, **121**, 663–675.

Brownlee, S. J., Schulte-Peljum, V., Raju, A., Mahan, K., Condit, C., & Orlandini, O. F., 2017. Characteristics of deep crustal seismic anisotropy from a compilation of rock elasticity tensors and their expression in receiver functions, *Tectonics*, **36**, 1835–1857.

Capdeville, Y., Guillot, L., & Marigo, J.-J., 2010. 2-D non-periodic homogenization to upscale elastic media for *P–SV* waves, *Geophys. J. Int.*, **182**, 903–922.

Červený, V., 2001. *Seismic Ray Theory*, Cambridge University Press.

Chadwick, P., Vianello, M., & Cowin, S. C., 2001. A new proof that the number of linear elastic symmetries is eight, *Journal of the Mechanics and Physics of Solids*, **49**, 2471–2492.

Chen, M., Tromp, J., Helmberger, D., & Kanamori, H., 2007. Waveform modeling of the slab beneath Japan, *J. Geophys. Res.*, **112**.

Christensen, N. I., 1966. Shear wave velocities in metamorphic rocks at pressures to 10 kilobars, *J. Geo-*

phys. Res., **71**(14), 3549–3556.

Crampin, S., 1987. Geological and industrial implications of extensive-dilatancy anisotropy, *Nature*, **328**, 491–496.

Diner, Ç., Kochetov, M., & Slawinski, M. A., 2010. On choosing effective symmetry classes for elasticity tensors, *Q. J. Mech. Appl. Math.*, **64**(1), 57–74.

Dziewonski, A. & Anderson, D., 1981. Preliminary reference Earth model, *Phys. Earth Planet. Inter.*, **25**, 297–356.

Eddy, C. L., Ekström, G., & Nettles, M., 2022. Three-dimensional seismic anisotropy in the Pacific upper mantle from inversion of a surface-wave dispersion data set, *Geophys. J. Int.*, **231**, 355–383.

Ekström, G., 2011. A global model of Love and Rayleigh surface wave dispersion and anisotropy, 25–250 s, *Geophys. J. Int.*, **187**, 1668–1686.

Fletcher, R., Du, X., & Fowler, P. J., 2009. Reverse time migration in tilted transversely isotropic (TTI) media, *Geophysics*, **74**(6), 179–187.

Forte, S. & Vianello, M., 1996. Symmetry classes for elasticity tensors, *J. Elasticity*, **43**, 81–108.

François, M., Geymonat, G., & Berthaud, Y., 1998. Determination of the symmetries of an experimentally determined stiffness tensor: application to acoustic measurements, *Int. J. Solids Structures*, **35**(31–32), 4091–4106.

Gaboret, C., Forte, A. M., & Montagner, J.-P., 2003. The unique dynamics of the Pacific Hemisphere mantle and its signature on seismic anisotropy, *Earth Planet. Sci. Lett.*, **208**, 219–233.

Gupta, A., 2025. Synthetic seismograms in support of "Navigating the space of seismic anisotropy for crystal and whole-Earth scales", Version 1.0 [Data set]. Zenodo https://doi.org/10.5281/zenodo.14736099.

Hadden, S. M. & Pratt, R. G., 2017. Full waveform inversion of crosshole data in tilted transversely isotropic media, 79th EAGE Conference & Exhibition, Paris France, 12-15 June 2017.

Helbig, K., 1994. *Foundations of Anisotropy for Exploration Scientists*, Pergamon.

Hess, H., 1964. Seismic anisotropy of the uppermost mantle under oceans, *Nature*, **203**(4945), 629–631.

Igel, H., Mora, P., & Riollet, B., 1995. Anisotropic wave propagation through finite-difference grids, *Geophysics*, **60**(4), 1203–1216.

Ji, S., Zhao, X., & Francis, D., 1994. Calibration of shear-wave splitting in the subcontinental upper mantle beneath active erogenic belts using ultramafic xenoliths from the Canadian Cordillera and Alaska, *Tectonophysics*, **239**, 1–27.

Jiang, F., Speziale, S., & Duffy, T. S., 2004. Single-crystal elasticity of grossular- and almandine-rich garnets to 11 GPa by Brillouin scattering, *J. Geophys. Res.*, **109**, 1–10.

Johnston, J. E. & Christensen, N. I., 1995. Seismic anisotropy of shales, *J. Geophys. Res.*, **100**(B4), 5991–6003.

Karato, S., Jung, H., Katayama, I., & Skemer, P., 2008. Geodynamic significance of seismic anisotropy of the upper mantle: New insights from laboratory studies, *Annu. Rev. Earth Planet. Sci.*, **36**, 59–95.

Kästner, K., Pierdominici, S., Elger, J., Zappone, A., Kück, J., & Berndt, C., 2020. Correlation of core and downhole seismic velocities in high-pressure metamorphic rocks: a case study for the COSC-1 borehole, Sweden, *Solid Earth*, **11**, 607–626.

Köhn, D., Hellwig, O., De Nil, D., & Rabbel, W., 2015. Waveform inversion in triclinic anisotropic media—a resolution study, *Geophys. J. Int.*, **201**, 1642–1656.

Komatitsch, D., Barnes, C., & Tromp, J., 2000. Simulation of anisotropic wave propagation based upon a spectral element method, *Geophysics*, **65**(4), 1251–1260.

Komatitsch, D., Liu, Q., Tromp, J., Süss, P., Stidham, C., & Shaw, J. H., 2004. Simulations of ground motion in the Los Angeles basin based upon the spectral-element method, *Bull. Seismol. Soc. Am.*, **94**(1), 187–206.

Laske, G. & Masters, G., 1998. Surface-wave polarization data and global anisotropic structure, *Geophys. J. Int.*, **132**, 508–520.

Liu, C. & Ritzwoller, M. H., 2024. Seismic anisotropy and deep crustal deformation across Alaska, *J. Geophys. Res. Solid Earth*, **129**, 1–22.

Liu, Q. & Gu, Y. J., 2012. Seismic imaging: From classical to adjoint tomography, *Tectonophysics*, **566-567**, 31–66.

Lokajíček, T. & Svitek, T., 2015. Laboratory measurement of elastic anisotropy on spherical rock samples by longitudinal and transverse sounding under confining pressure, *Ultrasonics*, **56**, 294–302.

Lokajíček, T., Vasin, R., Svitek, T., Petružálek, M., Kotrlý, M., Turková, I., Onysko, R., & Wenk, H. R., 2021. Intrinsic elastic anisotropy of Westerly granite observed by ultrasound measurements, microstructural investigations, and neutron diffraction, *J. Geophys. Res. Solid Earth*, **126**, 1–23.

Long, M. D. & Becker, T. W., 2010. Mantle dynamics and seismic anisotropy, *Earth Planet. Sci. Lett.*, **297**, 341–354.

Ma, Z. & Masters, G., 2015. Effect of earthquake locations on Rayleigh wave azimuthal anisotropy models, *Geophys. J. Int.*, **203**, 1319–1333.

Mainprice, D., 2007. Seismic anisotropy of the deep earth from a mineral and rock physics perspective, in *Seismology and Structure of the Earth*, vol. 1 of **Treatise on Geophysics**, pp. 289–321, eds Romanowicz, B. & Dziewonski, A., Elsevier.

Maupin, V. & Park, J., 2007. Wave propagation in anisotropic media, in *Seismology and Structure of the Earth*, vol. 1 of **Treatise on Geophysics**, pp. 289–321, eds Romanowicz, B. & Dziewonski, A., Elsevier.

Mehrabadi, M. M. & Cowin, S. C., 1990. Eigentensors of linear anisotropic elastic materials, *Q. J. Mech. Appl. Math.*, **43**(1), 15–41.

Militzer, B., Wenk, H.-R., Stackhouse, S., & Stixrude, L., 2011. First-principles calculation of the elastic moduli of sheet silicates and their application to shale anisotropy, *American Mieneraolgist*, **96**, 125–137.

Montagner, J.-P., 2007. Upper mantle structure: global isotropic and anisotropic elastic tomography, in *Seismology and Structure of the Earth*, vol. 1 of **Treatise on Geophysics**, pp. 559–589, eds Romanowicz, B. & Dziewonski, A., Elsevier.

Montagner, J.-P. & Nataf, H.-C., 1986. A simple method for inverting the azimuthal anisotropy of surface waves, *J. Geophys. Res.*, **91**(B1), 511–520.

Montagner, J.-P. & Tanimoto, T., 1991. Global upper mantle tomography of seismic velocities and anisotropies, *J. Geophys. Res.*, **96**(B12), 20,337–20,351.

Monteiller, V. & Chevrot, S., 2011. High-resolution imaging of the deep anisotropic structure of the San Andreas Fault system beneath southern California, *Geophys. J. Int.*, **186**, 418–446.

Nataf, H.-C., Nakanishi, I., & Anderson, D. L., 1984. Anisotropy and shear velocity heterogeneity in the upper mantle, *Geophys. Res. Lett.*, **11**, 109–112.

Oh, J.-W., Shin, Y., Alkhalifah, T., & Min, D.-J., 2020. Multistage elastic full-waveform inversion for tilted transverse isotropic media, *Geophys. J. Int.*, **223**, 57–76.

Okaya, D., Rabbel, W., Beilecke, T., & Hasenclever, J., 2004. P wave material anisotropy of a tectono-metamorphic terrane: An active source seismic experiment at the KTB super-deep drill hole, southeast Germany, *Geophys. Res. Lett.*, **31**.

Operto, S., Virieux, J., Ribodetti, A., & Anderson, J. E., 2009. Finite-difference frequency-domain modeling of viscoacoustic wave propagation in 2D tilted transversely isotropic (TTI) media, *Geophysics*, **74**(5), 75–95.

Panning, M. P. & Nolet, G., 2008. Surface wave tomography for azimuthal anisotropy in a strongly reduced parameter space, *Geophys. J. Int.*, **174**, 629–648.

Peter, D., Komatitsch, D., Luo, Y., Martin, R., Le Goff, N., Casarotti, E., Le Loher, P., Magnoni, F., Liu, Q., Blitz, C., Nissen-Meyer, T., Basini, P., & Tromp, J., 2011. Forward and adjoint simulations of seismic wave propagation on fully unstructured hexahedral meshes, *Geophys. J. Int.*, **186**, 721–739.

Pros, Z. & Babuška, V., 1968. An apparatus for investigating the elastic anisotropy on spherical rock samples, *Studia Geophysica et Geodaetica*, **12**, 192–198.

Russell, J. B., Gaherty, J. B., Mark, H. F., Hirth, G., Hansen, L. N., Lizarralde, D., Collins, J. A., & Evans, R. L., 2022. Seismological evidence for girdled olivine lattice-preferred orientation in oceanic lithosphere and implications for mantle deformation processes during seafloor spreading, *Geochem. Geophy. Geosyst.*, **23**, 1–22.

Sieminski, A., Liu, Q., Trampert, J., & Tromp, J., 2007. Finite-frequency sensitivity of body waves to anisotropy based upon adjoint methods, *Geophys. J. Int.*, **168**, 368–389.

Tape, C. & Gupta, A., 2024. Lattice diagrams of elastic maps, Version 1.0 [Data set]. Zenodo `https://doi.org/10.5281/zenodo.11073093`.

Tape, W. & Tape, C., 2021. Elastic symmetry with beachball pictures, *Geophys. J. Int.*, **227**, 970–1003.

Tape, W. & Tape, C., 2022. Two complementary methods of inferring elastic symmetry, *J. Elasticity*, **150**, 91–118.

Tape, W. & Tape, C., 2024. A reformulation of the Browaeys and Chevrot decomposition of elastic maps, *J. Elasticity*, **156**, 415–454.

Tian, D., Uieda, L., Leong, W. J., Fröhlich, Y., Schlitzer, W., Grund, M., Jones, M., Toney, L., Yao, J., Tong, J.-H., Magen, Y., Materna, K., Belem, A., Newton, T., Anant, A., Ziebarth, M., Quinn, J., & Wessel, P., 2024. PyGMT: A Python interface for the Generic Mapping Tools, v0.13.0 . Zenodo `https://doi.org/10.5281/zenodo.13679420`.

VanderBeek, B. P. & Faccenda, M., 2021. Imaging upper mantle anisotropy with teleseismic P-wave delays: insights from tomographic reconstructions of subduction simulations, *Geophys. J. Int.*, **225**, 2097–2119.

Verma, R. K., 1960. Elasticity of some high-density crystals, *J. Geophys. Res.*, **75**(2), 757–766.

Vestrum, R. W., Brown, R. J., & Easley, D. T., 1996. From group or phase velocities to the general anisotropic stiffness tensor, in *Seismic Anisotropy*, pp. 101–140, eds Fjær, E., Holt, R. M., & Rathore, J. S., Society of Exploration Geophysicists, Tulsa, Oklahoma, USA.

Walker, A. M., Forte, A. M., Wookey, J., Nowacki, A., & Kendall, J.-M., 2011. Elastic anisotropy of D$''$ predicted from global models of mantle flow, *Geochem. Geophy. Geosyst.*, **12**(10), 1–22.

Wessel, P., Luis, J. F., Uieda, L., Scharroo, R., Wobbe, F., Smith, W. H. F., & Tian, D., 2019. The generic mapping tools version 6, *Geochem. Geophy. Geosyst.*, **20**(11), 5556–5564.

Ye, W., Huang, X., Han, L., Vatankhah, S., & Zhang, P., 2023. Bayesian inverse scattering theory for multiparameter full-waveform inversion in transversely isotropic media, *Geophysics*, **88**(3), 91–109.

APPENDIX A: ONE CANNOT CALCULATE DIRECTLY WITH THE VOIGT MATRIX

Voigt notation is standard in the literature for representing elastic materials derived from laboratory measurements (Almqvist & Mainprice 2017; Brownlee et al. 2017); this includes all of the examples in our Section 3. The Voigt matrix of an elastic map $\mathbf{T}$ is the matrix representation $[\mathbf{T}]_{\Sigma\Upsilon}$ of $\mathbf{T}$ with respect to the two different bases Σ and Υ (Tape & Tape 2021, Sections S5.1, S5.4). (They are bases for the space $\mathbb{M}$ of 3×3 symmetric matrices—stresses and strains. Here the notation Σ has nothing to do with symmetry classes.) If Σ and Υ had been the same and orthonormal, then inner products (hence distances and angles) of Voigt matrices would have been the same as the inner products of their elastic maps. That is, the mapping $\mathbf{T} \rightarrow [\mathbf{T}]_{\Sigma\Upsilon}$ would have preserved inner products. Of course the fact that $\Sigma \neq \Upsilon$ and that neither is orthonormal does not in itself mean that inner products are not preserved. We find, however, from examining hundreds of pairs of measured elastic maps, that the angles between the Voigt matrices range from 30% lower to 5% higher than the angles between the corresponding elastic maps. The Voigt matrix has other disadvantages as well. The eigenvalues of the Voigt matrix, for example, need not be the same as those of its elastic map. Appendix B1 has an example.

Several authors have recognized the inadequacy of the Voigt matrix. Thus Mehrabadi & Cowin (1990); Bóna et al. (2007); Diner et al. (2010) instead used the representation $[\mathbf{T}]_{\Phi\Phi}$, where the orthonormal basis Φ (our notation) for $\mathbb{M}$ is that of (Mehrabadi & Cowin 1990, eq. 3.2) or (Tape & Tape 2021, eq. S23). Our representation $[\mathbf{T}]_{\mathbb{B}\mathbb{B}}$ in this paper is slightly preferable to $[\mathbf{T}]_{\Phi\Phi}$ in that it gives simpler expressions for the reference matrices (Table S1) and for the associated projection formulas (Tape & Tape 2024, eq. 84). For example, the diagonal forms for the ISO and CUBE reference matrices mean that the diagonal entries are eigenvalues.

Eqs. S28 and S29 of Tape & Tape (2021) convert $[\mathbf{T}]_{\mathbb{B}\mathbb{B}}$ to $[\mathbf{T}]_{\Sigma\Upsilon}$ and vice versa.

APPENDIX B: CLOSEST ISOTROPIC MAP TO T

The closest isotropic map to $\mathbf{T}$ plays a central role in our approach, because it is at the end of most pathways considered (irrespective of node sequence and node mode) and because it provides a primary measure of anisotropy β_{ISO} via Equation (6) with $\Sigma = \text{ISO}$.

Let $T' = [\mathbf{K}_{\text{ISO}}]_{\mathbb{BB}}$ be the matrix of $\mathbf{K}_{\text{ISO}}$ with respect to the basis $\mathbb{B}$. Its (normally) non-zero entries T'_{ij} are (Tape & Tape 2024, eq. 84a):

$$
\begin{aligned}
T'_{11} = T'_{22} = T'_{33} = T'_{44} = T'_{55} &= \tfrac{1}{5}\left(T_{11} + T_{22} + T_{33} + T_{44} + T_{55}\right) \\
T'_{66} &= T_{66}.
\end{aligned}
$$

Thus there are six non-zero entries, of which at most two are distinct. The matrix is diagonal, so the eigenvalues are obvious:

$$
\begin{aligned}
\lambda_1 &= T'_{11} \\
\lambda_6 &= T'_{66}
\end{aligned}
$$

Eigenvalue $\lambda_1 = 2\mu$, where μ is the shear modulus, and eigenvalue $\lambda_6 = 3\kappa$, where κ is the bulk modulus. Then one can directly obtain $\mu = T'_{11}/2$ and $\kappa = T'_{66}/3$ from the entries of a general $T = [\mathbf{T}]_{\mathbb{BB}}$.

B1 The equivalent in Voigt notation

As mentioned in Appendix A, the Voigt matrix of $\mathbf{K}_{\text{ISO}}$ is the matrix $C' = [\mathbf{K}_{\text{ISO}}]_{\Sigma\Upsilon}$; it is the 6×6 matrix that maps the strain vector $[\boldsymbol{\epsilon}]_{\Upsilon}$ to the stress vector $[\boldsymbol{\sigma}]_{\Sigma}$. The non-zero entries C'_{ij} are

$$
\begin{aligned}
C'_{11} = C'_{22} = C'_{33} &= (f + 2a)/3 \\
C'_{12} = C'_{13} = C'_{23} &= (f - a)/3 \\
C'_{44} = C'_{55} = C'_{66} &= a/2,
\end{aligned}
$$

where $C'_{ij} = C'_{ji}$ and

$$
\begin{aligned}
a = \lambda_1 &= \tfrac{2}{15}\left(C_{11} - C_{12} - C_{13} + C_{22} - C_{23} + C_{33} + 3(C_{44} + C_{55} + C_{66})\right) \\
f = \lambda_6 &= \tfrac{1}{3}\left(C_{11} + 2C_{12} + 2C_{13} + C_{22} + 2C_{23} + C_{33}\right),
\end{aligned}
$$

and where the C_{ij} (unprimed) are the entries of the Voigt matrix of $\mathbf{T}$.

Thus there are twelve (normally) non-zero entries of C', of which at most three are distinct. The entries of C' are unwieldy in terms of the C_{ij}. Also, the six eigenvalues of C' are $\{\lambda_1, \lambda_1, \lambda_1/2, \lambda_1/2, \lambda_1/2, \lambda_6\}$, which are not the eigenvalues $\{\lambda_1, \lambda_1, \lambda_1, \lambda_1, \lambda_1, \lambda_6\}$ of the closest isotropic map to $\mathbf{T}$.

APPENDIX C: WAVEFIELD SIMULATIONS IN ANISOTROPIC MODELS

Estimation of elastic parameters from laboratory samples or portions of the Earth generally require measurements of seismic waves. We perform 3D wavefield simulations using two different sets of homogeneous anisotropic models, shown in Figures 9 and 11. Our choice of domain is motivated by modeling crustal and uppermost mantle properties in subduction zones, and therefore we place the earthquake hypocenter at 75 km depth (such as within a subducting slab) and consider stations at the surface. For the homogeneous properties, we assume variations on the An0 albite feldspar crystal analyzed in Brown et al. (2016). This material has trivial symmetry ($\beta_{\text{MONO}} = 3.8°$, as in Figure 3) and therefore requires all 21 parameters to be specified, no matter how the material is oriented. The feldspar density is 2623 kg/m^3 Brown et al. (2016). We model the entire domain as homogeneous feldspar, which is appropriate for the laboratory scale but unrealistic for representing the Earth structure. Alternatively we could have scaled the dimensions to laboratory scales, in which case the seismograms in Figures 9 and 11 would have similar shapes but a much shorter time scale (and therefore higher frequencies).

We use Specfem3D to perform the seismic wavefield simulations (Komatitsch et al. 2000, 2004; Peter et al. 2011). In order to avoid any late-arriving, spurious reflections from the boundaries, we use a large computational domain. Our domain is 624×624 km at the surface and 312 km in depth. The mesh contains 121.5 million brick-like elements and 1.042 billion global gridpoints. Each simulation takes about 180 minutes on 1872 computing cores. The simulations are accurate down to periods of about 1.0 s. The source is a vertically oriented CLVD, which has the advantage of azimuthal symmetry while generating both P and S waves. (A vertical point force would be a suitable alternative.) The grid of stations is displayed in Figure S9.

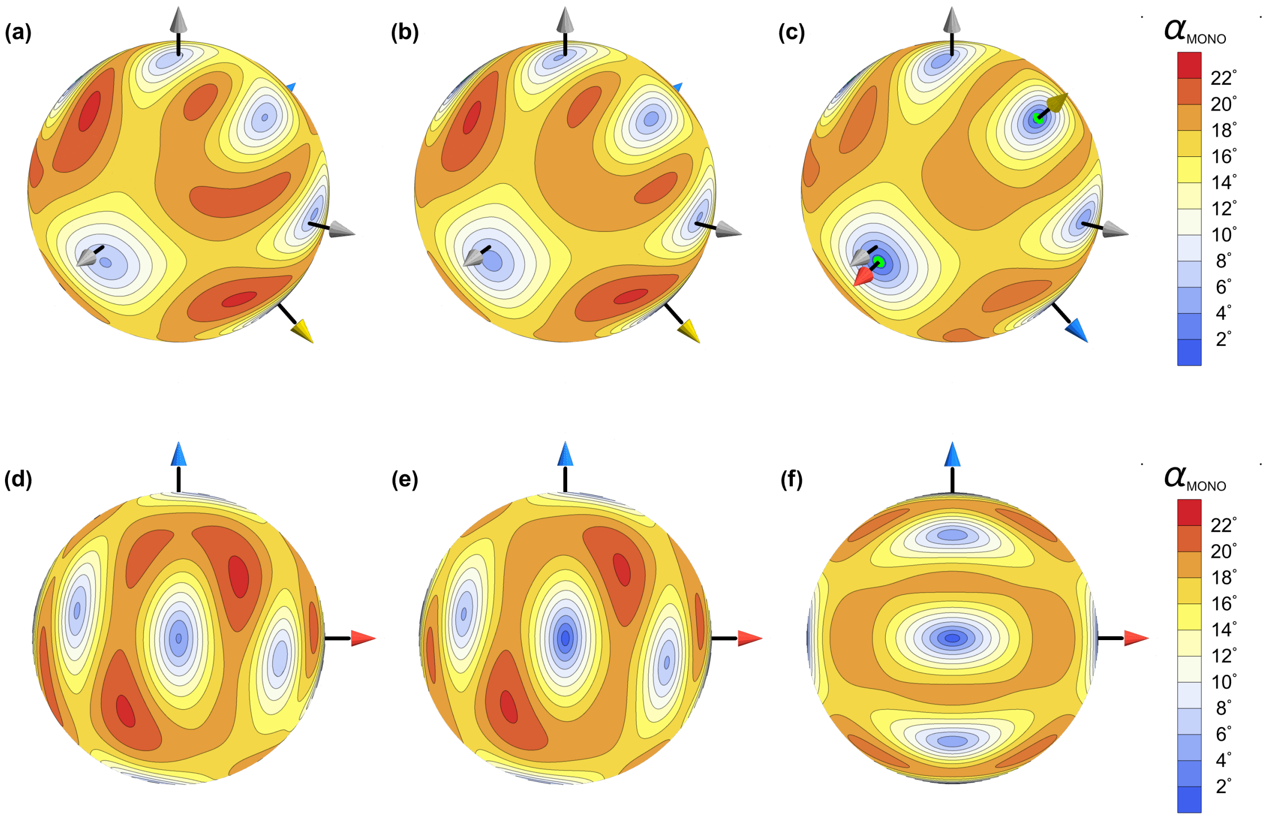

Figure 1. Visualization of elastic maps using the monoclinic angular distance function α_{MONO}. For each point $\mathbf{v}$ on the sphere, $\alpha^{\mathbf{T}}_{\text{MONO}}(\mathbf{v})$ is the angle between the elastic map $\mathbf{T}$ and the closest elastic map to $\mathbf{T}$ having a 2-fold symmetry axis at $\mathbf{v}$. (a) α_{MONO}-sphere for the An0 elastic map $\mathbf{T}$ of Brown et al. (2016), which has trivial symmetry. This map, which we refer to as BrownAn0, is featured in Figures 2, 3, and Figures 7–12. (b) α_{MONO}-sphere for the closest monoclinic map $\mathbf{K}_{\text{MONO}}$ to $\mathbf{T}$. The angle from $\mathbf{T}$ is $\beta_{\text{MONO}} = \angle(\mathbf{T}, \mathbf{K}_{\text{MONO}}) = 3.8°$. (c) α_{MONO}-sphere for the closest orthorhombic map $\mathbf{K}_{\text{ORTH}}$ to $\mathbf{T}$. The angle from $\mathbf{T}$ is $\beta_{\text{ORTH}} = \angle(\mathbf{T}, \mathbf{K}_{\text{ORTH}}) = 6.4°$. In each of (a)-(c) the gray arrows are the coordinate axis vectors $\mathbf{e}_1$ (left), $\mathbf{e}_2$ (right), and $\mathbf{e}_3$ (up). The red, blue, and yellow arrows are the columns $\mathbf{u}_1$, $\mathbf{u}_2$, and $\mathbf{u}_3$ of a rotation matrix $U = U^{\mathbf{T}}_{\Sigma}$ as described in connection with Eq. 5; in diagrams (a) and (b) the matrix U is $U^{\mathbf{T}}_{\text{MONO}}$ and in (c) it is $U^{\mathbf{T}}_{\text{ORTH}}$. (d)-(f) Same elastic maps as in (a)-(c), but seen from viewpoints that better display their symmetry. Each view is down the (yellow) $\mathbf{u}_3$ axis, but the yellow arrow has been removed in order to see the contour details. It follows from Tape & Tape (2024, Table 2) that the antipodal points $\pm\mathbf{u}_3 = \pm U^{\mathbf{T}}_{\text{MONO}}\mathbf{e}_3$ are 2-fold points of $\mathbf{K}_{\text{MONO}}$. The monoclinic symmetry of $\mathbf{K}_{\text{MONO}}$ is best seen in (e). Likewise, $\pm\mathbf{u}_i = \pm U_{\text{ORTH}}\mathbf{e}_i$, $i = 1, 2, 3$, are 2-fold points of $\mathbf{K}_{\text{ORTH}}$ (green dots in (c)). The elastic maps $\mathbf{T}$, $\mathbf{K}_{\text{MONO}}$, and $\mathbf{K}_{\text{ORTH}}$ have zero (d), one (e), and three (f) 2-fold axes, as expected for TRIV, MONO, and ORTH symmetry.

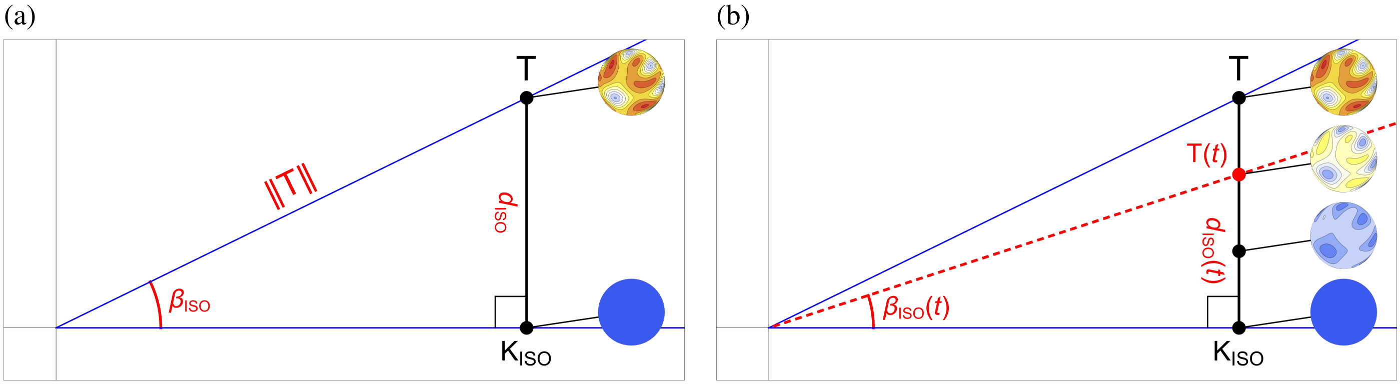

Figure 2. (a) The relation between the angle $\beta_{\mathrm{ISO}} = \angle(\mathbf{T}, \mathbf{K}_{\mathrm{ISO}})$ and the distance $d_{\mathrm{ISO}} = \|\mathbf{T} - \mathbf{K}_{\mathrm{ISO}}\|$ for an elastic map $\mathbf{T}$ and its closest ISO map $\mathbf{K}_{\mathrm{ISO}}$. The horizontal axis represents all isotropic maps. The elastic map $\mathbf{T}$ is BrownAn0, for which $\beta_{\mathrm{ISO}} = 26.0°$. (b) Parameterization $\mathbf{T}(t)$ (Eq. 10) of the direct path from $\mathbf{T}$ to $\mathbf{K}_{\mathrm{ISO}}$. The four spheres (elastic maps) shown on the path are for $t = 0$ ($\mathbf{T}$: top), $t = 1/3$, $t = 2/3$, and $t = 1$ ($\mathbf{K}_{\mathrm{ISO}}$: bottom). The corresponding values of $\beta_{\mathrm{ISO}}(t)$ are 26.0°, 18.0°, 9.2°, and 0°. As t tends to 1, both $d_{\mathrm{ISO}}(t)$ and $\beta_{\mathrm{ISO}}(t)$ tend to zero, and $\mathbf{T}(t)$ tends to $\mathbf{K}_{\mathrm{ISO}}$ (solid blue). Angles in these 2D diagrams are in fact angles between elastic maps and hence are calculated as angles between 6×6 symmetric matrices.

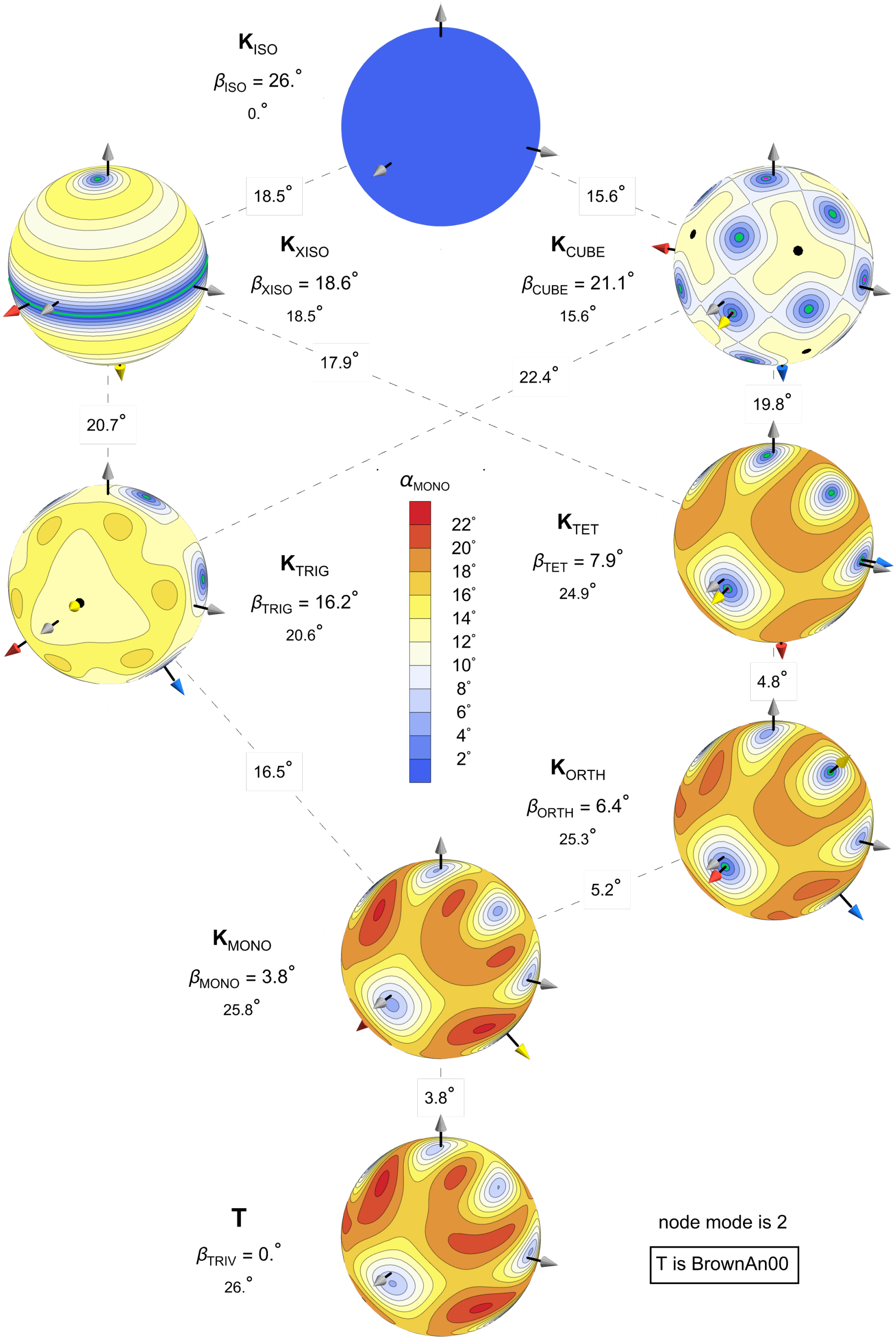

Figure 3. Lattice diagram of elastic maps: Visualization of an elastic map $\mathbf{T}$, at bottom, and the closest elastic map $\mathbf{K}_\Sigma$ to it having symmetry (at least) Σ: monoclinic (MONO), orthorhombic (ORTH), tetragonal (TET), trigonal (TRIG), transverse isotropic (XISO), cubic (CUBE), isotropic (ISO). On the sphere for $\mathbf{K}_\Sigma$, the green dots make up the zero-contour, which consists of the 2-fold symmetry axes of $\mathbf{K}_\Sigma$ and therefore determines its symmetry group. The spheres for $\mathbf{T}$, $\mathbf{K}_{\text{MONO}}$, and $\mathbf{K}_{\text{ORTH}}$ are the same as in Figure 1a,b,c. The angle β_Σ next to each sphere is the angular distance from $\mathbf{T}$ to $\mathbf{K}_\Sigma$. Each angle listed below β_Σ is $\angle(\mathbf{K}_{\text{ISO}}, \mathbf{K}_\Sigma)$. The angle listed between spheres is the angular distance between the corresponding maps.

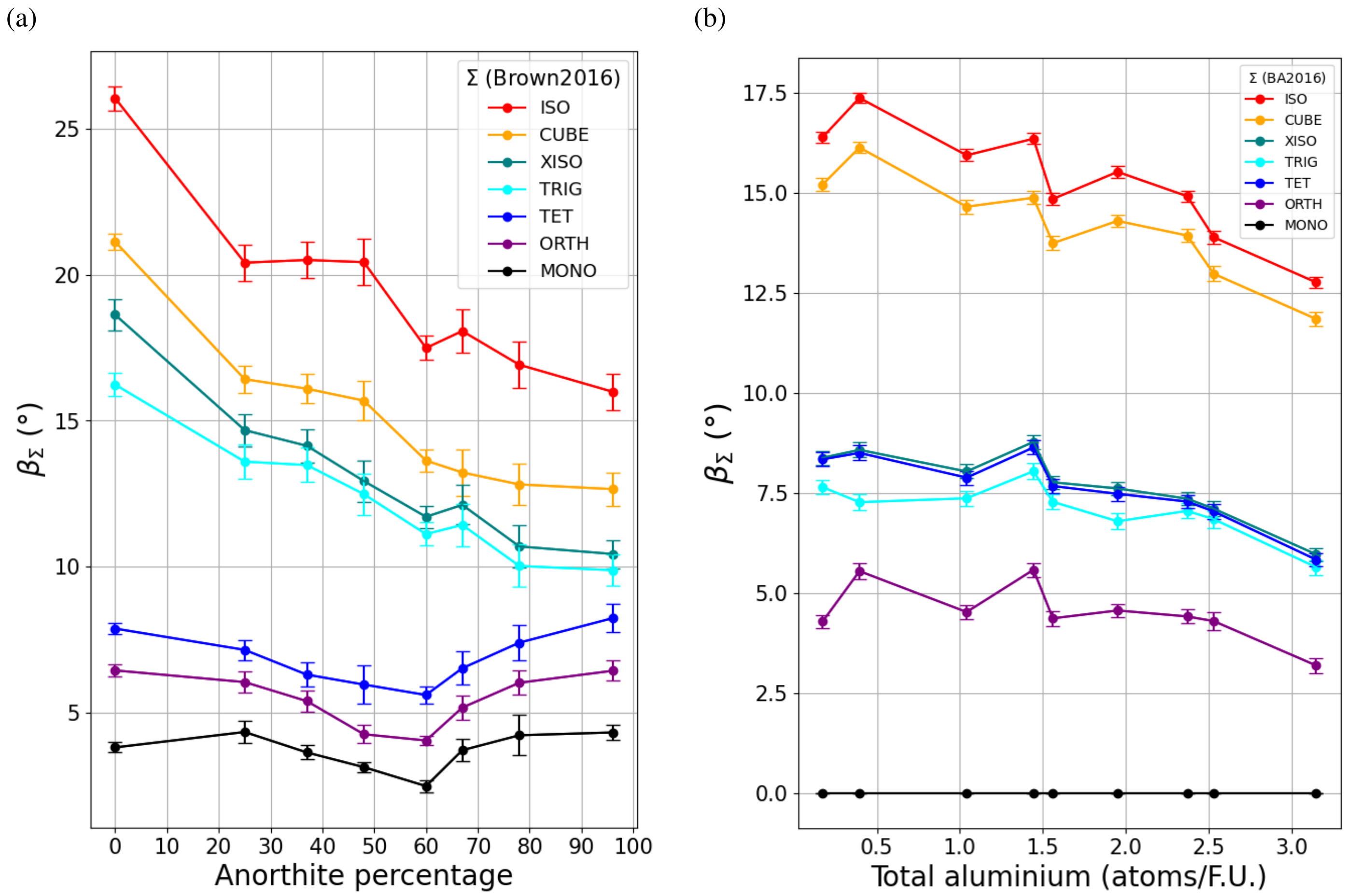

Figure 4. Two examples of the dependence of anisotropy on the chemical composition of crystals. For each elastic map, we calculate 1000 realizations using the published uncertainties for the C_{ij}. For each set of 1000 maps, we determine the closest Σ-maps for MONO, ORTH, TET, TRIG, XISO, CUBE, and ISO, and then calculate the corresponding β_Σ. The vertical uncertainty estimates are $\pm 2\sigma$. (a) Representation of the 8 elastic maps of Table 2 of Brown et al. (2016). Each map has 21 parameters and is for a feldspar crystal having a different percentage of anorthite. (b) Representation of the 9 monoclinic elastic maps from Table 3 of Brown & Abramson (2016). Each map has 13 parameters (monoclinic) and is for a different amphibole crystal.

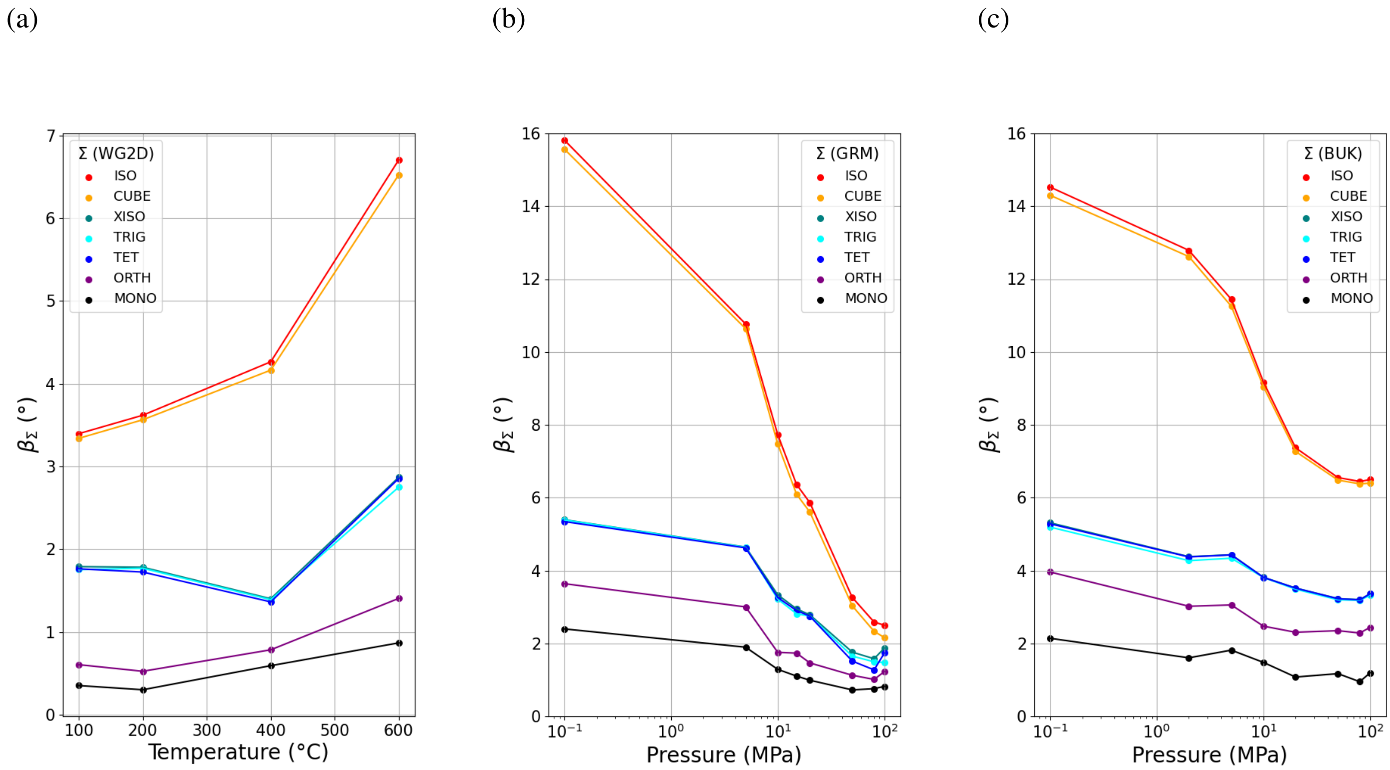

Figure 5. Dependence of elastic symmetry on temperature and pressure, represented by β_Σ angles. (a) Westerly granite dependence on temperature for a fixed pressure of 5 MPa; data from the published supplement of Lokajíček et al. (2021). The results—especially $\beta_{\rm ISO}$ (red)—depict increasing anisotropy with temperature. (b) Grimsel granite dependence on pressure; data from Table 4 of Aminzadeh et al. (2022). (c) Bukov migmatized gneiss dependence on pressure; data from Table 3 of Aminzadeh et al. (2022).

(a)

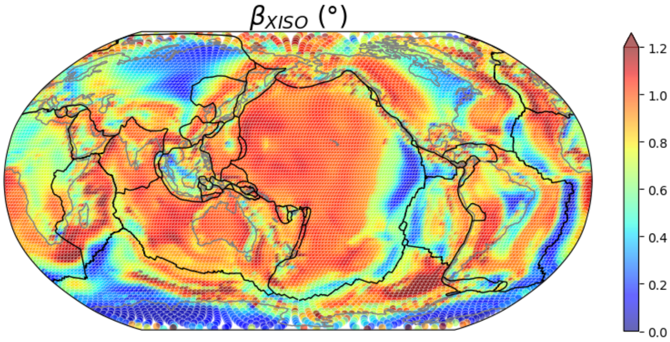

(b)

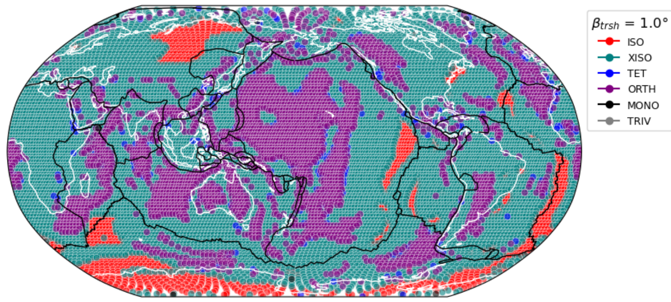

Figure 6. (a) Global plot of β_{XISO} for the global flow model `safs417nc3_er` at 200 km depth (Becker et al. 2008). The global flow model is provided as a set of 14,512 elastic maps. For each map we calculate its closest XISO-map and β_{XISO}. Figure S7 shows other β_{Σ} global plots. (b) Global plot of the symmetry class assigned to each elastic map. This procedure assumes a node sequence (see legend: TRIV-MONO-ORTH-TET-XISO-ISO) and a threshold value of $\beta_{\mathrm{trsh}} = 1.0°$.

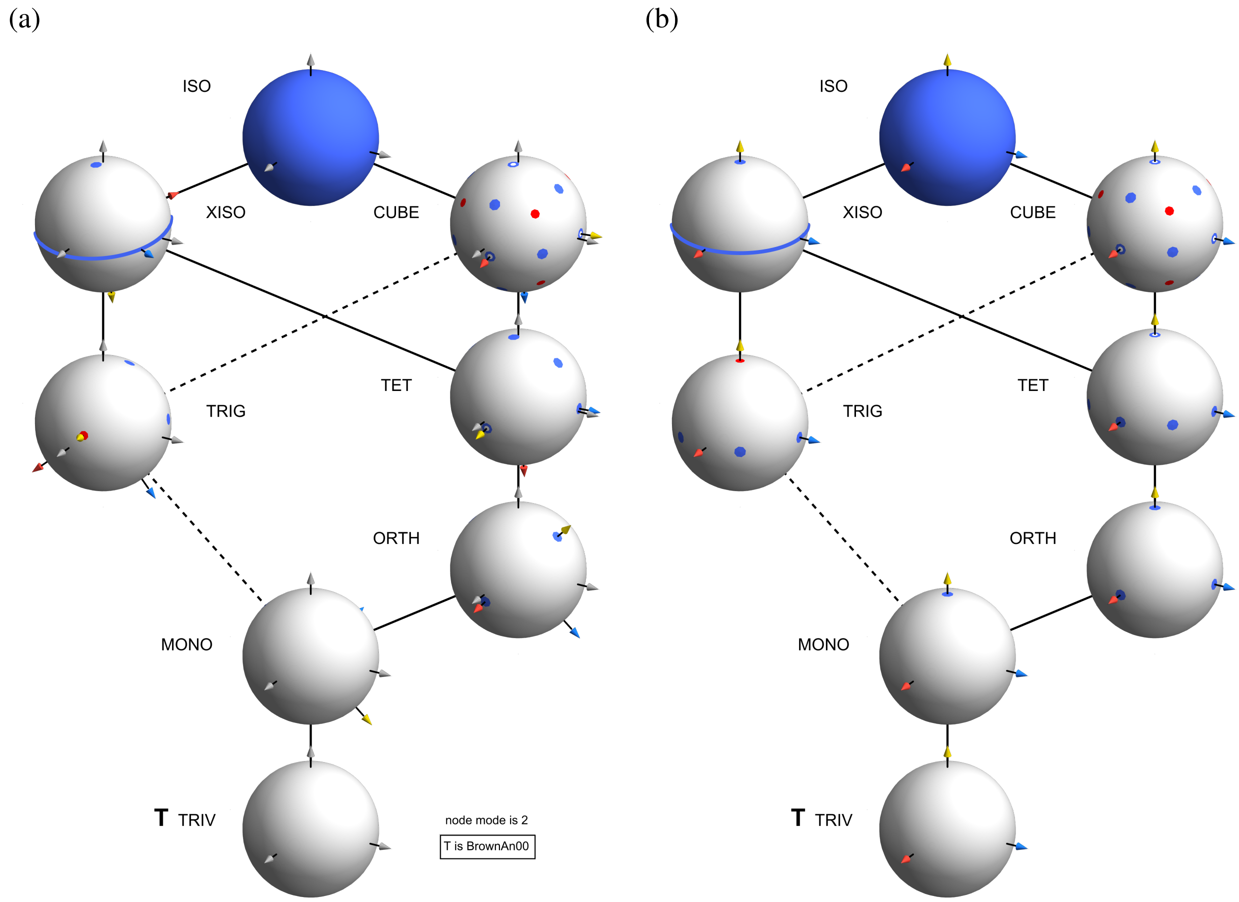

Figure 7. Two sets of eight elastic symmetry groups. Each group is determined by a rotation matrix U and one of the eight Σ; see Section 4.1 for more on U. On each sphere the blue dots are the 2-fold points—the points where the 2-fold axes of the symmetry group intersect the sphere. The red dots are likewise the 3-fold points, and the white-inside-blue dots are the 4-fold points. The configuration of the 2-fold points (blue) determines the symmetry group and thus can be regarded as a picture of it. The gray arrows are the coordinate axis vectors for $\mathbf{e}_1$ (left), $\mathbf{e}_2$ (right), and $\mathbf{e}_3$ (up). The colored arrows are the columns of U: $\mathbf{u}_1$ (red), $\mathbf{u}_2$ (blue), and $\mathbf{u}_3$ (yellow). (a) Like Figure 3, hence $U = U_\Sigma$, but here only the zero-contour of $\alpha^{\mathbf{K}_\Sigma}_{\mathrm{MONO}}$ is shown—the 2-fold points of the symmetry group. (b) Same as (a) but with $U = I$ for each node of the lattice. See Section 4.1 for details.

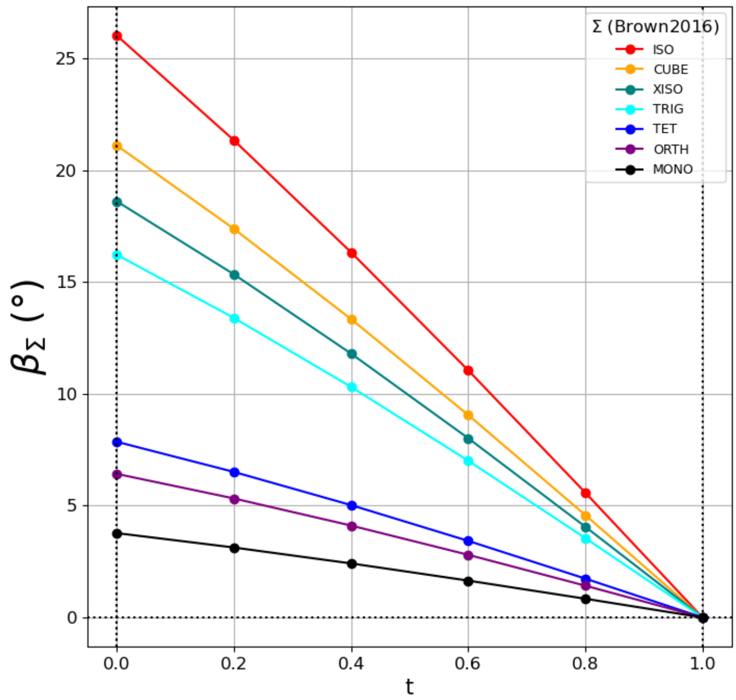

Figure 8. Beta curves for the direct path from $\mathbf{T}$ to $\mathbf{K}^{\mathbf{T}}_{\text{ISO}}$, the closest isotropic map to $\mathbf{T}$. The plots are of the function $\beta^{\mathbf{T}(t)}_{\Sigma} = \angle\left(\mathbf{T}(t),\, \mathbf{K}^{\mathbf{T}(t)}_{\Sigma}\right)$, where $\mathbf{T}(t)$ is as in Eq. 10. The map $\mathbf{T}(0) = \mathbf{T}$ is BrownAn0, featured in Figures 1–3. For each Σ, values of $\beta^{\mathbf{T}(t)}_{\Sigma}$ (colored dots) were plotted for $t = 0, 0.2, 0.4, \ldots, 1.0$. With six values of t and seven Σ, a total of 42 calculated dots appear, with each dot obtained via minimization to find $\mathbf{K}^{\mathbf{T}(t)}_{\Sigma}$. The seven values of $\beta^{\mathbf{T}}_{\Sigma}$ (far left) are displayed next to the spheres in Figure 3; they range from $\beta^{\mathbf{T}}_{\text{MONO}} = 3.8°$ to $\beta^{\mathbf{T}}_{\text{ISO}} = 26.0°$.

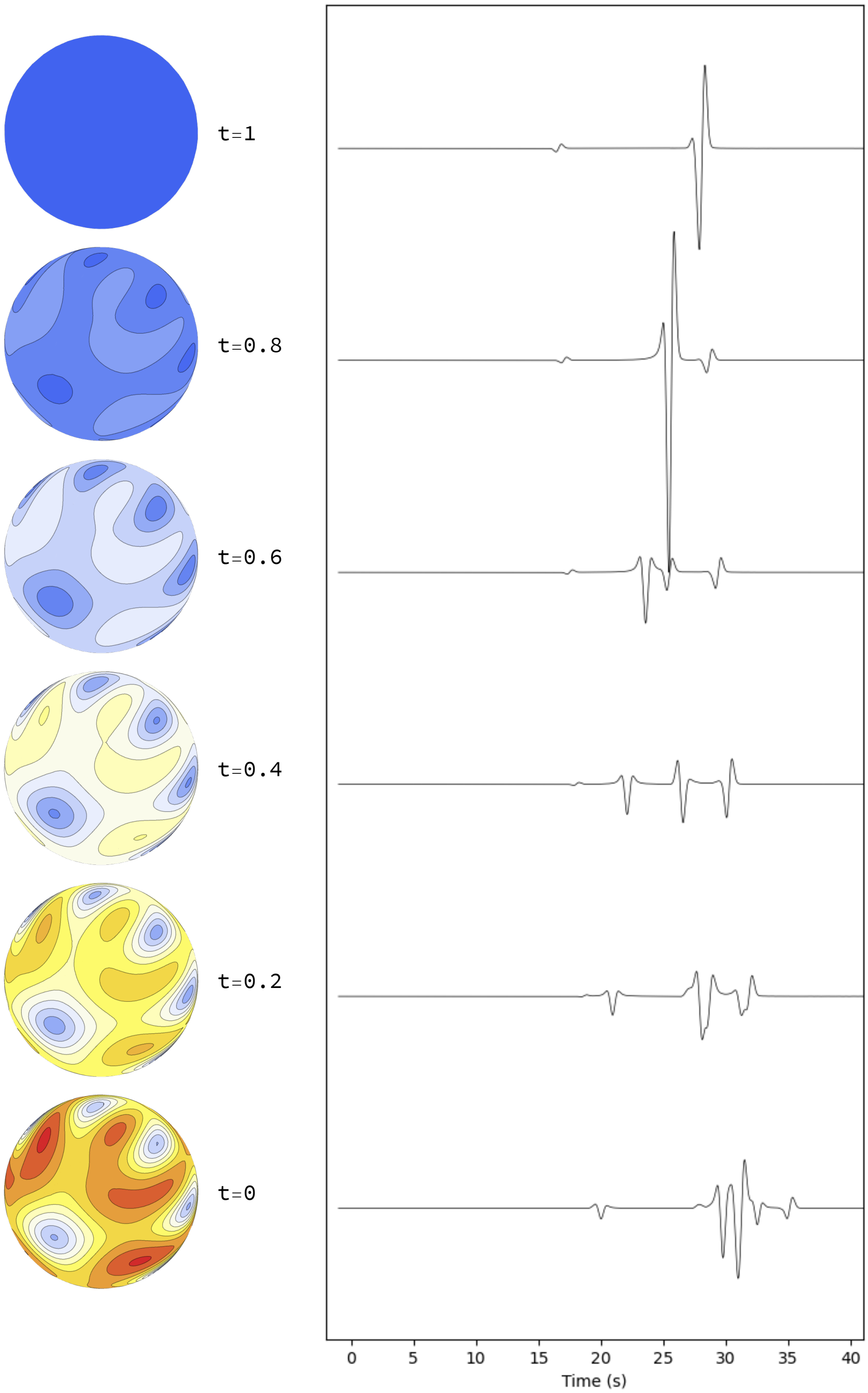

Figure 9. Influence of decreasing anisotropy on a synthetic seismogram computed in a three-dimensional model of a homogeneous anisotropic medium (Appendix C). Six simulations are performed, one for each homogeneous medium. (*Left*) $\alpha_{\rm MONO}$-spheres depicting the elastic maps for the homogeneous media. The six elastic maps $\mathbf{T}(t)$ are those used in Figure 8; they are on the direct path from $\mathbf{T}$ to $\mathbf{K}_{\rm ISO}$, so again the $t = 0$ map is BrownAn0 (bottom), and the $t = 1$ map is the closest isotropic map to it (top). (*Right*) Vertical component of ground velocity for an example station at the surface (epicentral distance 83 km and azimuth 25°) for a source at 75 km depth. The seismograms are normalized by the absolute maximum amplitude of all displayed seismograms. Choosing a different station may result in very different seismograms, since the waves will propagate in a different direction through the homogeneous anisotropic medium.

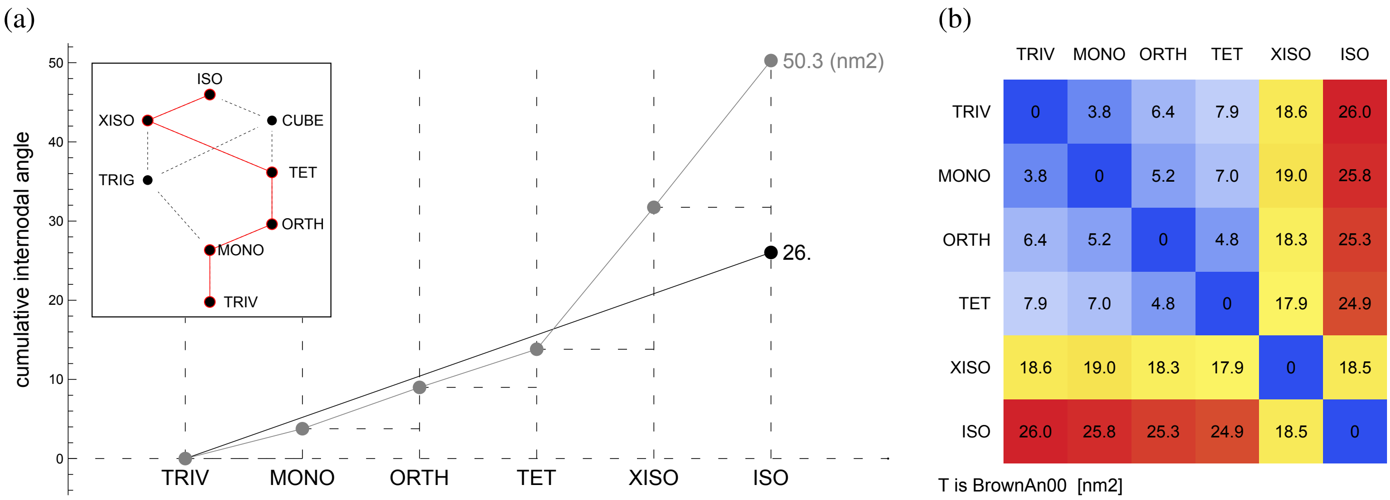

Figure 10. Cumulative internodal angle curves illustrated for one example node sequence. The example map $\mathbf{T}$ is BrownAn0 (Figures 1–3). (a) Cumulative curves for node mode nm2 (gray) in comparison with the direct path (black). The cumulative curve has an angular length of $50.3°$, while the direct path is $26.0°$. The sequence of lattice nodes from TRIV to ISO is shown on the x-axis and depicted in the inset lattice diagram; see also Figure 3. Figure S3 displays three other node sequences and two additional node modes for comparison. (b) Corresponding matrix of internodal angles for node mode 2. The five values in the first off-diagonal are internodal angles displayed in Figure 3. The five non-zero values in the top row are β_Σ angles in Figure 3. See Section 4.7 for details.

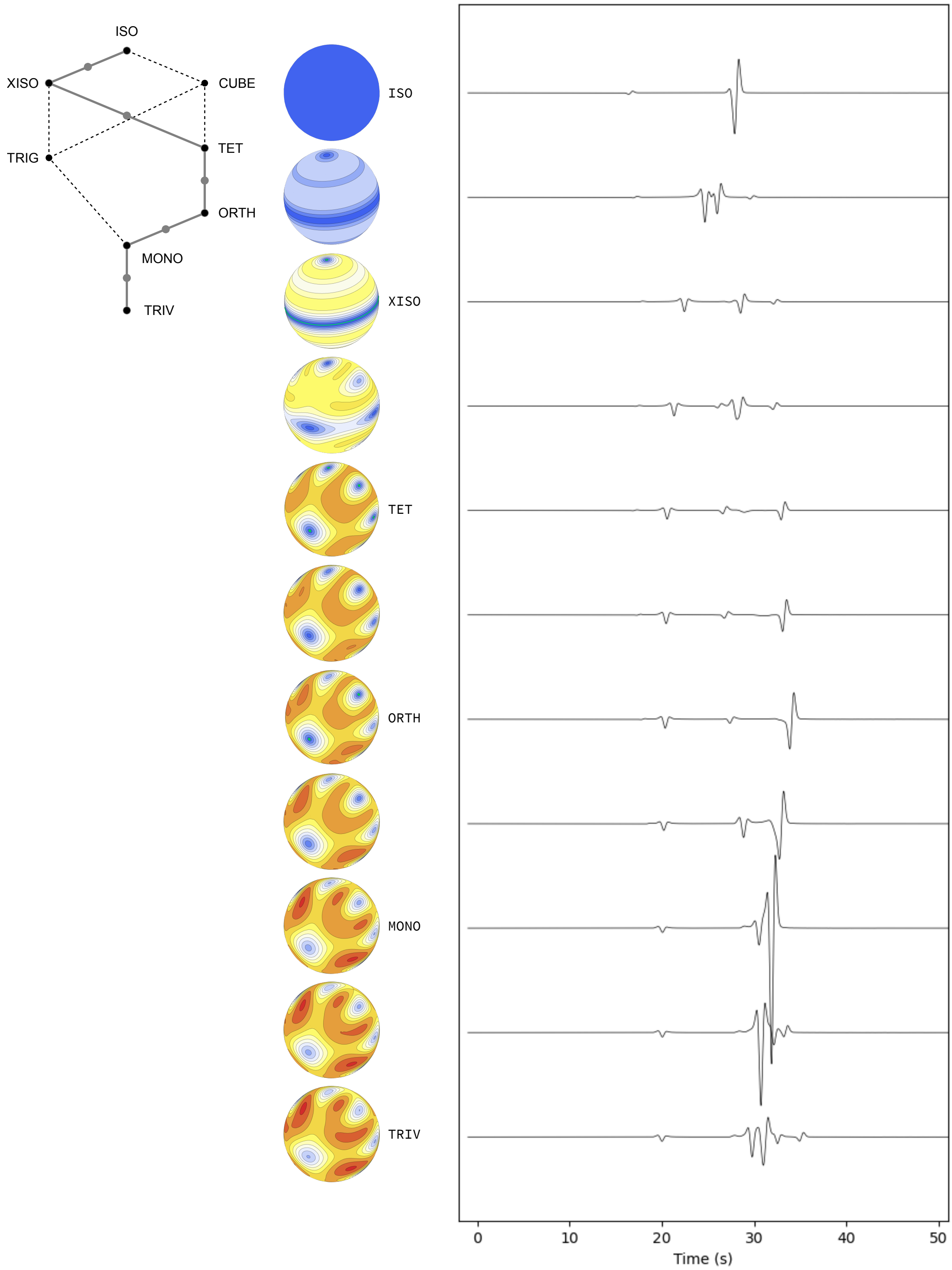

Figure 11. Influence of decreasing anisotropy on a synthetic seismogram—similar to Figure 9—but, whereas in Figure 9 the path from $\mathbf{T}$ (BrownAn0) to $\mathbf{K}^{\mathbf{T}}_{\mathrm{ISO}}$ was direct, here the path follows a lattice node sequence. (*Left*) Chosen lattice node sequence, with one elastic map between each pair of adjacent nodes. The 11 dots represent 11 elastic maps. (*Center*) α_{MONO}-spheres for the 11 elastic maps. Six of these ($\mathbf{K}^{\mathbf{T}}_{\Sigma}$) are also displayed in Figure 3, which also shows the color scale. (*Right*) Vertical component of ground velocity for the same station and source as in Figure 9. Each seismogram is computed in a homogeneous halfspace represented by the α_{MONO}-sphere to the left. The synthetic seismograms are normalized by the absolute maximum amplitude of all displayed seismograms.

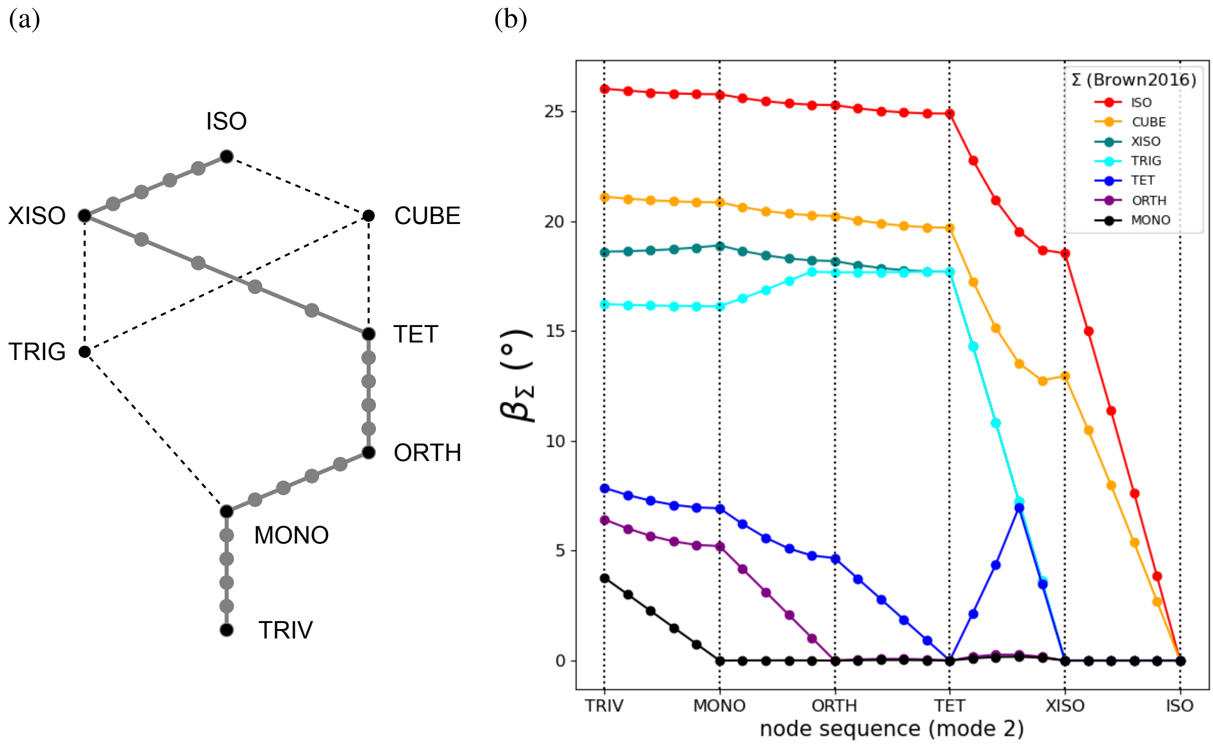

Figure 12. Beta curves with base maps varying from $\mathbf{T}$ (BrownAn0) to $\mathbf{K}^{\mathbf{T}}_{\text{ISO}}$, the closest isotropic map to $\mathbf{T}$. The node sequence is shown in (a), and the node mode is 2, meaning that at each node Σ the elastic map is $\mathbf{K}^{\mathbf{T}}_{\Sigma}$. For any elastic map $\mathbf{S}$, the angle $\beta^{\mathbf{S}}_{\Sigma} = \angle\left(\mathbf{S}, \mathbf{K}^{\mathbf{S}}_{\Sigma}\right)$ is a measure of how far $\mathbf{S}$ is from having (at least) symmetry Σ. The angle $\beta^{\mathbf{T}_i}_{\Sigma}$ was calculated for the 26 maps $\mathbf{T}_i$ shown as dots on the path in (a) and for seven Σ (not shown is $\beta^{\mathbf{T}_i}_{\text{TRIV}} = 0°$). Specifically, $\mathbf{T}_1 = \mathbf{T},\ \mathbf{T}_6 = \mathbf{K}^{\mathbf{T}}_{\text{MONO}}, \ldots, \mathbf{T}_{26} = \mathbf{K}^{\mathbf{T}}_{\text{ISO}}$. The horizontal axis in (b) should be regarded as the same as the path in (a), but straightened out. Although most of the behavior in the figure is not guessable initially, one feature is easily understood: Since, for example, $\mathbf{T}_{11} = \mathbf{K}^{\mathbf{T}}_{\text{ORTH}}$ itself has ORTH symmetry, then $\beta^{\mathbf{T}_{11}}_{\text{ORTH}} = 0°$. Likewise, $\beta^{\mathbf{T}_{16}}_{\text{TET}} = 0°$, etc. Compare the seemingly exotic beta curves here with those in Figure 8, which was for the direct path from $\mathbf{T}$ to $\mathbf{K}^{\mathbf{T}}_{\text{ISO}}$; how one gets from one point to another in the space of elastic maps matters hugely. With 26 maps $\mathbf{T}_i$ and seven Σ, a total of 182 minimizations were required to calculate all of the $\mathbf{K}^{\mathbf{T}_i}_{\Sigma}$. Other choices of node modes (Figure S4) and node sequences (Figure S5) are possible.